2D TEM-MODE THz QUASIOPTICS

By

STEVEN M. COLEMAN

Bachelor of Science

Oklahoma State University

Stillwater, OK

2000

Submitted to the Faculty of the
Graduate College of the
Oklahoma State University
in partial fulfillment of
the requirements for
the Degree of
DOCTOR OF PHILOSOPHY
May, 2005

2D TEM-MODE THz QUASIOPTICS

Dissertation Approved:

Daniel R. Grischkowsky

Dissertation Advisor

R. Alan Cheville

James C. West

James P. Wicksted

A. Gordon Emslie

Dean of the Graduate College

This work is dedicated to Almalene Hill-Foster, my hero.
June 17th, 1931 – January 19th, 2005

Acknowledgements

I would like to thank my advisor, Dr. Daniel Grischkowsky for welcoming me into his THz research group and setting me in pursuit of truth and beauty. It has been an honor and a privilege to have developed this work under his watchful eye. I am grateful to Dr. Grischkowsky for his guidance, wisdom, and patience.

I would like to thank the other members of my advisory committee: Dr. Alan Cheville, Dr. James West, and Dr. James Wicksted. Thank you for helping to fine tune my research so that it might obtain the esteem of your approval. I am a better scientist for your many contributions.

I would like to express my sincerest thanks to Matthew Reiten. Matt's role in this work was integral and extensive. Matt helped me with making many of the measurements in this document, particularly those using the scanning, fiber-coupled receiver. Without Matt's experimental ability and intellectual curiosity, the full capability of the PPT transmitter may also never have been discovered. Matt, you are an exemplary human being and I value our friendship dearly.

To Stacee Harmon and Adam Bingham, I cannot express to each of you how grateful I am for your understanding, helpful advice, and excellent proofreading. You are very special friends and I have certainly extracted more from our friendship than I have returned. Thank you for always being there for me.

My thanks also go to Rod Brakhage. Without his careful, precise, and extremely rapid workmanship, many of the devices demonstrated in this work may not have been developed. Oft was the time I would submit a drawing to Rod at 9 am, only to find an expertly crafted finished device ready before lunch. Rod, you have been an invaluable colleague.

To my parents Shirley and Robert Coleman, you have served as consistent examples for my development. Your support and trust in me has never faltered. Thank you for guiding my life not by mandate or script, but by example. This work is in no small part your doing. Thank you.

To my dear wife, Amy, whom I cannot find appropriate words to thank: You are the epitome of love and kindness. You have seen me through my darkest hours, sickness and health, prosperity and sadness throughout the course of this work, and my adult life. To say that I could not have done this without you is an understatement; you are my better half.

To my grandmother, Almalene Hill-Foster, you have been the perfect example of kindness, fortitude, love, courage, and ability. You have inspired me to seek a diverse skill set and have set an example to which I have done my best to aspire. It is to you that this work is dedicated. Thank you for sacrificing our time together that I might complete it.

Finally, I would like to thank God and the host of contributions from my lab mates, family, and friends that have gone otherwise unmentioned in these acknowledgements.

Table of Contents

List of Figures

List of Symbols

2D	two-dimensional
A	amplitude, usage as in text
Al	aluminum
B	susceptance (Siemens)
b	parallel plate waveguide plate spacing (m)
c	speed of light in free space (2.998 x 10^8 m/s)
DC	zero frequency
f	frequency (Hz)
F-chip	coplanar THz transmitter with 80 μm spaced transmission line
FDTD	finite-difference time-domain
FWHM	full-width at half-maximum
G	frequency independent component of guide absorption
GaAs	Gallium Arsenide
GVD	group velocity dispersion
H	Planck's constant (6.626 x 10^{-36} J·s)
j	imaginary number ($\sqrt{-1}$)
k_x	x-directed propagation constant (m^{-1})
k_0	propagation constant of freespace ($2\pi/\lambda$).
L	length, usage as specified in text (m)

LDPE	low-density polyethylene
LT	low-temperature (grown)
m	TM mode number (dimensionless)
N	number of carriers
N_m	power coupling coefficient to the m^{th} TM-mode.
P	average power
PC	photoconductive
PPWG	parallel plate waveguide
PPT	parallel plate THz transmitter
r_{perp}	reflectivity of metal surface for perpendicular polarization
RF	radio frequency
SI	semi-insulating
Si	Silicon
SOS	silicon-on-sapphire
TEM	transverse electromagnetic
THz-TDS	THz time-domain spectroscopy
Ti	titanium
TM_m	m^{th} transverse magnetic guided mode
w	1/e beam waist radius (m)
Z	impedance (Ohms)
α	absorption coefficient (Nepers or Decibels/unit length)
Γ	fluence (J/m^2)
Δ	difference, usage as specified in text

ε_0	permittivity of free space (8.854 x 10^{-12} F/m)
ε_r	relative permittivity (dimensionless)
η	wave impedance of free space (377 Ω)
θ	angle, usage as specified in text (radians)
λ	free space wavelength (m)
λ_{diff}	diffraction wavelength (m)
μ_0	permeability of free space (4π x 10^{-7} H/m)
σ	conductivity (Siemens/m)
σ_a	absorption cross-section (m^{-2})
φ	phase angle, usage as specified in text (radians)
ω	radial frequency (radians/s)
$\in_n$	Neumann's number (dimensionless)

Chapter 1

Introduction

Guided waves at THz frequencies are an important topic in the burgeoning field of ultrafast THz radiation. THz guiding structures are of interest for high-speed interconnect devices at the board and chip level [1], sensitive waveguide THz time-domain spectroscopy (THz-TDS) [2], and for emerging applications including quantum cascade lasers [3]. Various guided-wave devices have been demonstrated at or near THz frequencies ranging from lithographically defined coplanar waveguides [4,5], to various geometries of dielectric and metal waveguides [6-9], and to parallel metal plate guides [10-12]. The parallel plate waveguide (PPWG) has been shown to be an ideal guiding structure, propagating ultra-wideband THz pulses in the TEM-mode with very low-loss and negligible group velocity dispersion (GVD). These properties are unaffected even when the guide is made to be flexible and formed into oddly shaped paths [11]. In addition, the parallel plate waveguide has the extremely important property of being a planar device. It is thus conceptually compatible with standard chip and circuit board fabrication techniques.

For various regions of the electromagnetic spectrum, planar guiding structures have received attention for their potential to incorporate devices of higher functionality thereby enabling them to act as more than simple guiding structures. This development is due to their compatibility with available planar production technologies. Quite often, the elements integrated in planar guiding structures are optical, being lenses, mirrors, or diffractive elements. At microwave frequencies, Mink et al. have demonstrated two-dimensional *quasi*optical elements incorporated within a dielectric slab waveguide [13,14]. These devices were considered for narrow band operation as planar resonators and as hybrid waveguide/beam guiding devices. At optical frequencies, the dielectric slab waveguide has been thoroughly exploited by many authors [15-22]. Integrated lenses of various types, mirrors, and diffractive elements have been demonstrated. At THz frequencies guiding structures that can manipulate radiation in a dielectric slab have also been demonstrated [23-25]. Flat and focusing "mirrors," diffractive slit elements, and guiding channels have been demonstrated within the slab. Thus, in various forms, it is the planar dielectric slab guide that has been proposed and demonstrated for integrating optical devices at frequencies ranging from microwave to the near-infrared.

However, dielectric slabs exhibit undesirable behaviors for guidance and manipulation of ultrafast THz pulses. Demonstrated dielectric slab devices exhibit substantial dispersion in the THz frequency range, which stretches a pulse in time [26]. Furthermore, the boundaries of a slab guide are such that the guided fields are not entirely contained within a particular layer. In general, this characteristic allows adjacent layers to couple to one another. However, much of this undesirable behavior can be eliminated if the slab is bound by two parallel metal plates, as in the case of the parallel plate guide of Mendis and Grischkowsky mentioned above [11].

In contrast to dielectric slabs, the low-loss, negligible dispersion, ease of fabrication, and surprisingly forgiving nature of parallel metal plate guides makes them ideal candidates for further development as functional planar THz guiding structures.

This dissertation extends the utility of parallel plate structures by incorporating passive quasioptical elements, sources, and detectors within the guiding layer. In this manner, a guiding structure is formed that behaves as a two-dimensional optical bench coupled with the robust and forgiving utility of a parallel plate guide. Unlike integrated optics in dielectric slabs, the quasioptical elements in our parallel plate guides behave as their standard 3D counterparts in free space. Thus, well-known optical theories may be immediately applied within the guiding structure. The functionality added by integrating quasioptical elements expands the capabilities of this already high-performance guiding structure, opening a new realm of possibilities for ultrafast THz circuits.

Scope of this Dissertation

This dissertation is arranged in five chapters. Chapter 2 provides a brief description of the proposed guiding structure. The applicability of standard theories is explained, and the benefits of the demonstrated structures over standard integrated optical elements are considered. Several curves are developed, plotted, and explained to facilitate rapid system development. First order approximations to fabrication tolerances and size constraints are also made.

Chapter 3 describes the construction of a THz bandwidth interconnect layer and the experimental arrangement used to investigate this layer. Simple reflective optics are incorporated in the layer to route a THz pulse within a plane. Data taken with these optics is analyzed to determine the influence of reflective quasioptical elements on absorption. Reflective quasioptics are shown to be a viable means of routing the signal through the THz interconnect layer with very low-loss due to absorption and no discernable mode-conversion over the frequency range of interest. A more complicated reflective focusing mirror is demonstrated to temporally and spatially compress a guided THz beam according to the expectations of the analogous 3D device in free space. Lastly, experiments are described where transmissive and diffractive quasioptical elements are demonstrated within the layer.

Chapter 4 describes the demonstration of an ultrafast THz source proposed for direct-excitation of the interconnect layer. The fabrication of the individual source dice is described in detail. The source is then investigated experimentally to determine its behavior. This behavior is compared to that of standard free space coupled sources due to the lack of guided wave sources/detectors. Unique attributes of this source are considered. The importance of the source lies in the fact that it forms a single point within the layer for point-to-point communication applications. As a preliminary demonstration of a second point in the communication scheme, a detector for the new planar guiding structure is demonstrated resulting in the first true TEM-mode all guided wave system operating at THz frequencies.

Chapter 5 summarizes this work, illustrating the new concepts and devices introduced in the course of this research. Future work and potential applications are proposed.

Chapter 2

2D TEM-mode Quasioptics

This chapter introduces a two-dimensional quasioptical structure, which may be considered as a two-dimensional optical table. This structure is based on parallel plate waveguides, which have been shown to exhibit low-loss TEM-mode propagation for frequencies to 4.5 THz and guided path lengths of up to 0.25 meters [10,11]. The structure proposed in this chapter extends the performance of PPWGs by incorporating various components between the plates. These components may be passive quasioptical devices such as mirrors, lenses, and diffractive elements, or they may be active such as sources and detectors. The passive components control the otherwise unguided dimension of the parallel plate guide and work as standard quasioptical elements in free space. The active elements in the layer act as communication nodes in the structure serving to generate and detect ultrafast TEM-mode THz radiation. The planar THz guiding structure considered in this document is composed of two plates with a sub-wavelength separation, which are assumed to be semi-infinite with respect to the THz beam. The guide is depicted in Figure 2.1 below. The incorporated lenses, mirrors, sources and detectors are to be placed between the metal plates.

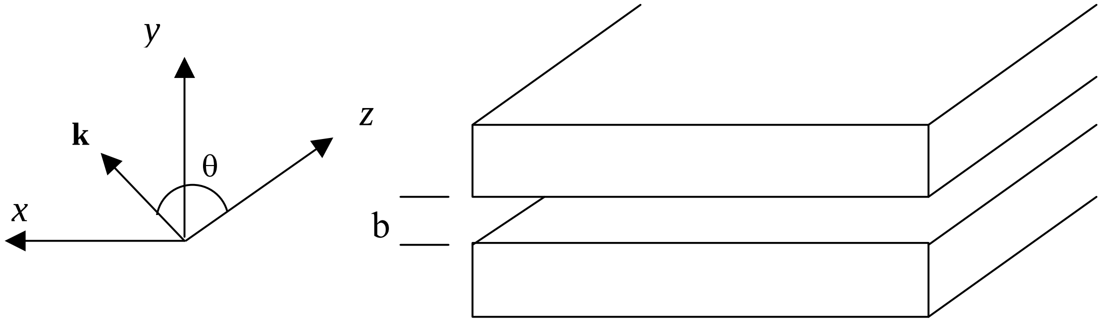

Figure 2.1: THz interconnect layer illustrating the rectangular coordinate system considered. Two metal plates are separated by a dielectric, typically dry air, of thickness b. θ lies in the *xz*-plane and **k** is the direction of wave propagation.

Background

As previously described, parallel plate waveguides are particularly useful for ultrafast THz pulse propagation as they support TEM-mode propagation. This is the fundamental mode of the guide allowing guided-wave propagation at all frequencies with the same phase accumulation as for the unbound dielectric for perfectly conducting plates. Fields in this mode have constant amplitude along the y-direction within the bounds of the guide. The electric field of the TEM-mode of a PPWG is typically considered to be polarized in the y-direction while uniform and infinite in the x-direction. However, the experiments of Mendis et al. illustrate that TEM-mode propagation is available for 2D beams, or fields with dependence in the x-direction. This situation is directly analogous to standard treatments of wave beams in free space [10,11,27]. Mendis et al. also demonstrated that propagation in the TEM-mode of the guide exhibits negligible dispersion despite the presence of a weakly frequency dependent loss process. Thus, previous experimental work demonstrates that we can consider a TEM-mode pulse traveling in a parallel plate waveguide with a finite envelope in the x-direction as a pulse in free space acted upon by a frequency dependent loss-process whose effect is negligible in phase. Given these facts, propagation in our planar TEM-mode guiding structure becomes quantitatively identical to 2D propagation in a low-loss, non-dispersive, unbound medium. Keeping these facts in mind, we consider the parallel plate structure further.

In the TEM-mode of a parallel plate waveguide, phase accumulation is identical to that of the unbound case of the enclosed dielectric [28, p113]. This fact is valid only for the TEM-mode of the PPWG with reasonable losses, which will be explained in more detail in a subsequent section. It is the equivalence of the phase accumulation of the TEM-mode of a PPWG to that of the unbound dielectric that allows the direct application of quasioptical techniques to guided radiation. This is in contrast to treatments of integrated optical elements in slab waveguides, which do not support TEM-mode propagation. In slab guides, the frequency dependent propagation of the guided mode(s) must be accounted for when considering integrated optical elements [18,22]. However, for our simple parallel plate structure, we may introduce a lens or mirror between the plates to obtain behavior that is directly analogous to the same device in an unbound 3D dielectric. Moreover, we may use reflective and diffractive optics to deflect radiation within the layer with direct comparison to a 3D device.

Thus, two-dimensional quasioptical elements incorporated within a parallel plate waveguide are considered, for the TEM-mode, as special cases of standard three-dimensional quasioptical elements in free space, where the direction of propagation is confined to a plane. With proper consideration, a 2D quasioptical table may be constructed by incorporating quasioptical elements within a PPWG. Unlike traditional integrated (quasi)optical elements in slab waveguide, the behavior of incorporated elements in a PPWG is shown in subsequent chapters to be well described by standard three-dimensional quasioptical treatments. The details of the Fourier and Gaussian beam optical treatments used are described well by many authors [27-32]. Two-dimensional treatments may be obtained in additional references [33-35]. These techniques will not be further considered, although they will be applied in subsequent chapters.

Guided Wave Angular Spectrum

In this section we examine the allowed angular spectrum of our guiding stucture as it compares to free space and other integrated optical structures. This treatment is prefaced by mentioning that, as demonstrated by Mendis and Grischkowsky, the frequency dependent attenuation of the layer has a negligible effect in phase. Mendis' analysis was performed using the nearly local Kramers-Kronig analysis, and holds for practically spaced PPWGs at THz frequencies [10,36]. Therefore, our waveguide simply appears as a low-loss dielectric, bound along one axis, and phase accumulation is the same as that for the unbound dielectric. In this case, we may represent an arbitrary wave in the half-space z>0, via an integral over an angular spectrum of appropriate amplitude plane waves:

$$E_y\left(x,y,z\right)=\iint A\left(k_x,k_y\right)e^{-j(k_x x+k_y y+k_z z)}dk_x dk_y \tag{2-1}$$

where the $e^{j\omega t}$ has been suppressed and the wave numbers correspond to the constraint equation:

$$k=\sqrt{k_x^2+k_y^2+k_z^2} \tag{2-2}$$

and

$$k=\frac{2\pi\sqrt{\varepsilon_r}}{\lambda}=k_0\sqrt{\varepsilon_r} \tag{2-3}$$

is the wave number in the enclosed dielectric. Unless specifically mentioned in the following treatments, it is assumed that the dielectric has a relative permittivity of unity, and $k=k_0$. The angular spectrum $A(k_x,k_y)$ is the Fourier transform of the amplitude profile $u(x,y;z=0)$. Typically in free space, k_y is continuous under the constraint equation (2-2). However, as our guided field is bound along the y-axis, k_y must be quantized in the typical form for PPWG modes [28]. For radiation propagating in the TEM-mode of the guide, k_y is set to zero and k can be rewritten in z-directed form:

$$k_z=\sqrt{k_0^2-k_x^2} \tag{2-4}$$

The guided TEM-mode field may now be written as:

$$E_y\left(x,z\right)=\int A\left(k_x\right)e^{-j\left(k_x x+k_z z\right)}dk_x \tag{2-5}$$

Our field is now represented by a continuous angular spectrum along a single axis and the problem is reduced to consideration in two-dimensions. This 2D plane wave spectrum is identical to 2D treatments in free space. It is precisely the elimination of the quantized and frequency dependent k_y by considering only the TEM-mode that discriminates our technique from other integrated optical techniques. In our structure propagating radiation appears as if it were in the unbound dielectric and has no variations in the y-direction. This is not true of integrated elements in a dielectric slab, which does not propagate the TEM-mode. In such cases the k_y component of the wave number must be accounted for by complicating standard optical treatments [22]. However, in our case we may use standard 2D quasioptical treatments as in an unbound dielectric. The fundamental limits of these treatments in our guide occur in situations where the phase constant of our layer does not match that of the unbound dielectric due to excessive losses. These situations will occur when the guide is fabricated from impractically lossy metals or the plate spacing is reduced to an impractical thickness, as described in a subsequent section.

Practical Concerns

This section is concerned with the practical design of two-dimensional integrated quasioptical structures for THz bandwidth operation. Important concepts are outlined in an intuitive manner and various curves for the design of these systems are plotted. This section is meant to serve as a starting point for the development of 2D quasioptical structures. It may be used to determine the plate spacing, guided path length, transverse size of integrated quasioptics, fabrication tolerances, and approximate dispersion for a 2D quasioptical structure. The design curves are derived from empirically derived information and simple theoretical considerations, and are not meant to substitute for detailed treatments of specific devices. The intent of this section is to provide an intuitive feel for the proposed integrated optical systems to facilitate their further development and provide a starting point for new system development.

Angular Spectrum, Cutoff Frequencies, and Ray Propagation

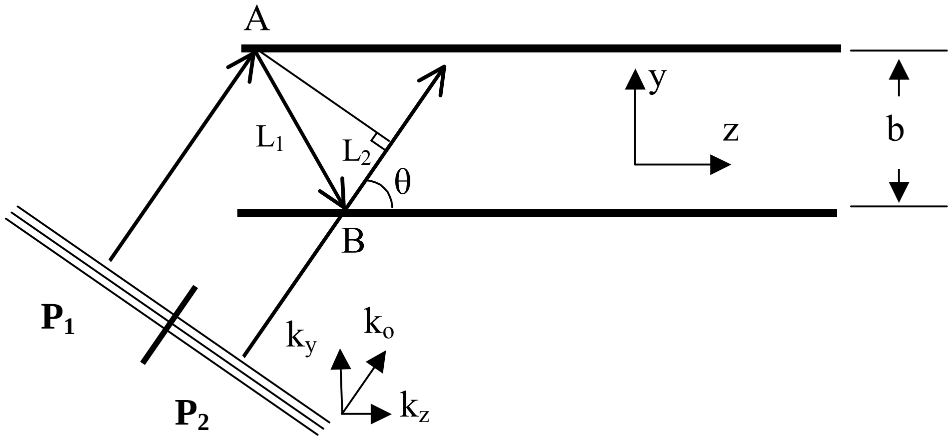

Figure 2.2: Ray optic depiction of a conceptual incident plane wave, and the ray optics representation of guided wave propagation. The components of the vector wavenumber are shown for a portion of the incident wavefront.

In this section we will look at parallel plate waveguide propagation in a somewhat different manner than that typically found in electromagnetics texts [e.g. 28]. We consider that waveguides work for the exact same reasons that mirrors and lenses work in free space. That is, the boundary conditions on the electric and magnetic fields in the guide are the same as those in free space. While it is true that the boundaries are much closer together for waveguides when compared to free space, the simple intuitive picture of ray propagation of guided wave radiation for reflections in the guide still holds. To illustrate this fact, we will for the moment consider the entire angular spectrum of Equation (2-1), this time neglecting k_x, where our fields are described by:

$$E_y(y,z) = \int A(k_y) e^{-j(k_y y + k_z z)} dk_y \tag{2-6}$$

These fields are infinite in the x-direction and propagate at some angle, θ, to the z-axis in the yz-plane. Figure 2.2 describes a single plane wave component of the angular spectrum $A(k_y)$. The parallel metal plates of our guiding structure, separated by a distance b, are excited by this plane wave. As shown in the figure, we conceptually divide the incident wavefront into two pieces, P_1 and P_2 to track their relative phases. These pieces must remain in phase, for instance at point B, for propagation in the waveguide to be allowed over any significant distance. To examine the relative phase of the components P_1 and P_2, we consider the difference in the distance traveled by each. This distance is given as:

$$\Delta L = L_1 + L_2 \tag{2-7}$$

which by some trigonometry becomes:

$$\Delta L = 2b \sin\theta \tag{2-8}$$

To consider the relative phase of each component, we look at the phase accumulation along the direction of propagation. This is always given as k_0 if the enclosed dielectric has a relative permittivity of one. Upon each reflection from the metal interface, which is assumed to be a perfect conductor, the wave is shifted in phase by $-\pi$ radians. Thus, the total relative phase of the two components is:

$$\Delta\phi = k_0 \Delta L - 2\pi \tag{2-9}$$

As mentioned before, the two components must be in phase at B, which means that the expression in (2-9) must be set equal to $2m\pi$, where m is a positive integer, resulting in:

$$k_0 \sin\theta = \frac{m\pi}{b} \tag{2-10}$$

Clearly the term on the left hand side of the expression is the y-component of the wavenumber, k_y, as shown in the figure. In this case k_y has been quantized through m. This value matches the eigen values solved for by direct application of Maxwell's equations in standard electromagnetics texts [28], revealing two facts: First, within the waveguide only radiation propagating at certain angles to the z-axis is allowed. Second, the ray consideration of propagating radiation containing y-directed elements is a valid and intuitive way of describing propagating guided mode radiation. It should be noted however that this treatment is limited in that it does not require the existence of two-plane waves propagating at oppositely signed angles, which is required to meet the boundary conditions in the guide. We will use the ray propagation method again in a subsequent section to treat unwanted tilt of incorporated elements.

Plate Spacing Design Curves

As described in the preceding section, a PPWG is capable of propagating an infinite spectrum of discrete modes. These modes are dependent on frequency and plate spacing through Equation (2-10). Where k_y is quantized by:

$$k_y = \frac{m\pi}{b} \quad m = 0, 1, 2, \ldots \tag{2-11}$$

By using only integer values of m we may plot the plate spacing of the PPWG as a function of frequency for the first ten higher-order TM modes. This curve is depicted in Figure 2.3.

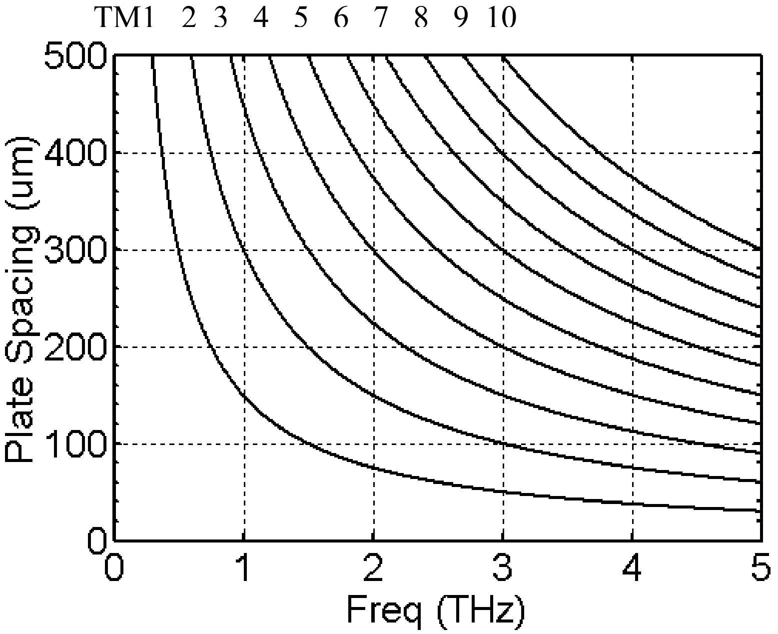

Figure 2.3: Minimum plate spacing as a function of frequency for the first 10 TM modes of an air filled parallel plate waveguide.

From Figure 2.3 we can quickly tell what plate spacing is necessary to achieve single-mode propagation below a given frequency, or how many modes may propagate in our spectrum for a given plate spacing. A guide with more than one mode in the bandwidth of interest is referred to as overmoded. As mentioned previously, it is the TEM (TM_0) mode propagation of our structure that differentiates its behavior from similar structures. Therefore, when overmoded guides are employed, special attention must be paid to the minimization of mode conversion processes. Special attention must also be paid in guide excitation so that a majority of the generated radiation couples to the TEM-mode.

Another parameter that is dependent on plate spacing is attenuation due to the finite conductivity of the metal walls of the guide. Figure 2.4 depicts the theoretical minimum attenuation spectrum in dB/cm for several plate spacings for the TEM-mode of a copper guide. As will be shown in a subsequent chapter, the experimentally achieved loss can currently be made less than twice the minimum value. Figure 2.3 and 2.4 may be used for engineering purposes in determining a plate spacing as a platform for 2D integrated optical structures. In pure theoretical form, there are no limits for minimum or maximum spacing of the guide plates. However, from a practical standpoint we must balance the deleterious effects of overmoding with those of absorption. The former limits the maximum thickness of our devices, while the latter limits the minimum thickness of our devices. Using Figure 2.4 we may determine the minimum thickness of our devices given an overall system power budget [29]. However, determining the maximum thickness is not as straight forward

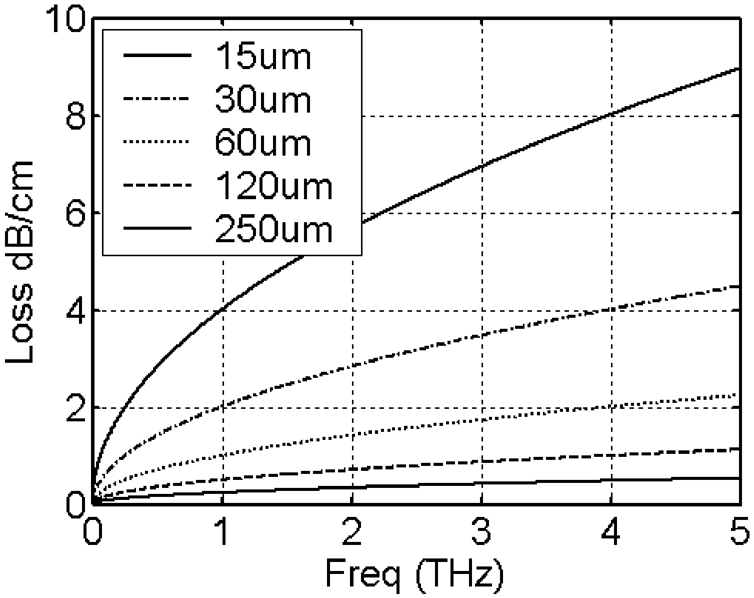

Figure 2.4: Minimum attenuation for a PPWG fabricated from copper plates at the indicated plate spacing.

The preceding treatments for guided wave propagation in our layer have neglected the effect of loss from the finite conductivity of the guide on dispersion. However, for long propagation distances, small plate spacing, and very large bandwidth signals these effects must be considered. These conditions may of course be interrelated. In the following consideration we are interested in the dispersion of a guide with a plate spacing on the order of 10-100 μm and the typical bandwidth used in our systems ranging from 100 GHz to 4.5 THz.

Absorption and dispersion are related through the Kramers-Kronig relations, which relate the real and imaginary components of a function**,** for instance permittivity. The exact calculation of dispersion from absorption using these relations requires that the frequency dependent absorption be known over the frequency range from 0 to infinity. However, the absorption of the guide given by equation (3-3) is not applicable over this broad range. Therefore, the typical analysis of THz PPWG data is performed using the nearly local approximation to the Kramers-Kronig relations [10,36]. This approximation is accurate provided that the variations in loss are smooth in frequency, such as that in equation (3-3). The frequency dependent phase velocity of a TEM-mode wave in our guide under this approximation is given as:

$$v_p(\omega) = v_0 - \frac{2v_0^2 G}{\pi} \int_{\omega_0}^{\omega} \omega^{-1.5} d\omega \qquad (2\text{-}12)$$

where v_0 is the phase velocity taken at some reference frequency and G is the frequency independent component of the absorption expression of (3-3). In practice the value of v_0 is derived from experimental data. Clearly the change in phase velocity due to absorption is in the form of a small correction to the dominant measured term. However, as phase velocity has not been measured as a function of plate spacing, we must approximate the value of v_0. For the TEM-mode of the guide this value should be well approximated by the free space speed of light, taken as $c=2.998\times10^8$ m/s. As such, we may calculate the correction value separate from $v_{0,}$ and determine the change in phase velocity over our bandwidth relative to the free space phase velocity. Figure 2.5 depicts this approximation illustrating the change in phase velocity of a guide in percent free space phase velocity as a function of plate spacing and frequency. The nearly local approximation is taken about the reference value of 2.25 THz, which is the center of our standard experimental spectra. The calculated absorption using equation (3-3) has been scaled by a factor of 1.5 to account for a slightly elevated experimentally observed absorption, as described in a subsequent section. From this figure, we may quickly determine the approximate range of phase velocities for a particular experimental configuration.

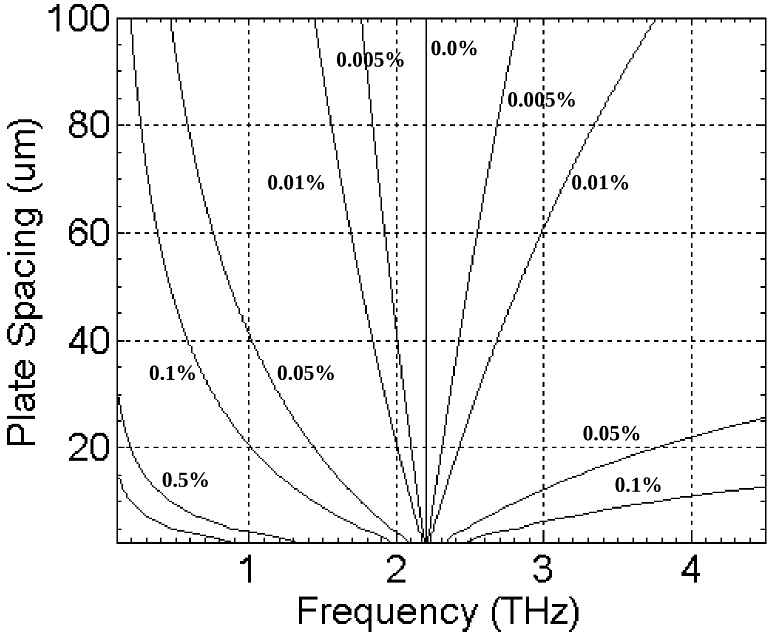

Figure 2.5: Absolute value of Δv_p in percent of free space velocity versus plate spacing and frequency for a signal with a bandwidth extending from 0.1 THz to 4.5 THz. Each line is an isocontour depicting constant dispersion.

The standard delay line step size of THz-TDS systems results in a change of path length of 10 μm and correspondingly a temporal resolution of 33 fs. For these systems, the change in phase velocity introduced by all but the shortest length (<1 mm) of waveguide will easily be detected. So a lower limit on plate spacing cannot be set based on THz-TDS system limitations. However, in reference [11], the dispersion of a 0.25 m length of 90 μm spaced copper waveguide is described to be negligible. This observation allows us to set a maximum on the lower limit of plate spacing by defining the product: $\%\Delta v_p L$. For radiation to propagate with no more dispersion than in the reference, $\%\Delta v_p L < (0.16\% \cdot 0.25\ \mathrm{m}) = 0.04\% \cdot \mathrm{m}$. For instance, for a length of guide of 0.04 m we may lower our plate spacing to 15 μm and achieve approximately the same negligible dispersive effects as in the reference over our bandwidth.

Allowable Element Tilt

The experimental demonstration of 2D quasioptics, described in the next chapter, was possible only after several less successful attempts. Many techniques were investigated for fabricating integrated reflective elements from cutting the metal mirror edges with razors and scissors, to shearing and direct CNC machining, and finally, specialized polishing procedures. Over the course of this initial experimentation it became clear that mirror edge structure was of primary importance. To illustrate this fact, measured reference and sample pulses are shown Figure 2.6. In the figure, the sample pulse has been reflected from four integrated flat mirrors and the reference pulse is a pass straight through a parallel plate guide. The left hand column shows a reference pulse through a straight parallel plate waveguide and a sample pulse from a waveguide with four integrated flat mirrors cut from aluminum sheeting using a razor wheel with no subsequent polishing. The right hand column in Figure 2.6 shows a reference pulse through a straight guide and a sample pulse from a guide also incorporating four flat mirrors. The mirrors are fabricated from copper sheeting using a specialized polishing process explained in Chapter 3. These pulses should not be compared based upon their absolute magnitude due to the use of differing experimental configurations for each case. The pulses from the 4 bounce case (lower) should be compared relative to the reference pulse (upper) for each experimental case. The improved signal of the right hand side is due to improved mirror fabrication techniques. These experimental observations spurred the development of better integrated quasioptical surfaces and the development of mathematical techniques for examining the effects of mirror imperfection.

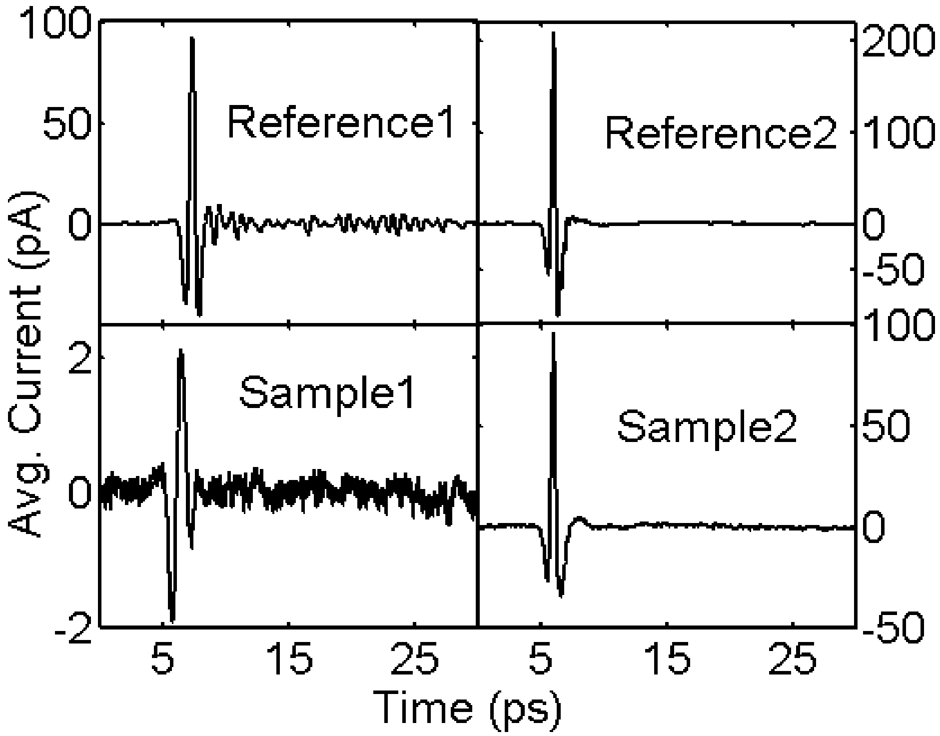

Figure 2.6: Influence of mirror fabrication technique on detected signals. Left column corresponds to reference and 4 bounces from integrated mirrors fabricated using a razor wheel. Right column corresponds to reference and 4 bounces from integrated mirrors fabricated using specialized polishing processes developed in this work.

In the following treatments, simple imperfections in fabricated 2D quasioptics are considered by examining the effects of tilting incorporated mirrors and lenses relative to the parallel metal plates comprising the layer. In particular, the coupling of radiation from the TEM-mode to higher-order propagating modes is considered. Thus, the results of this section are particularly relevant when an overmoded guide is chosen using Figure 2.3. In general, consideration of the conversion between modes by imperfections within a waveguide requires very detailed treatments [37,38]. However, the following simple treatment is meant to help determine the allowable fabrication tolerances on the tilt of integrated quasioptical elements.

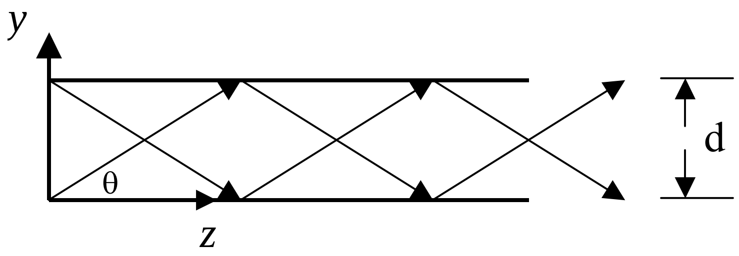

Figure 2.7: Conceptual model of higher-order mode propagation in a parallel plate guide as a sum of two plane waves bouncing between the plates.

We begin this section with the simple ray description of modal propagation in a waveguide. The electric field of the mth mode of the TM-mode spectrum of the PPWG may be written as:

$$E_y^m = A_m \cos\left(k_y y\right) e^{-jk_z z} \tag{2-13}$$

where $k_y = m\pi/b$. Rewriting this field in exponential form:

$$E_y^m = \frac{A_m}{2}\left[e^{-j\left(k_z z + k_y y\right)} + e^{-j\left(k_z z - k_y y\right)}\right] \tag{2-14}$$

Using this equation, we may consider a propagating higher-order mode wave as a sum of two uniform plane waves propagating at opposite angles to the guide plates. This view of propagation is depicted in Figure 2.7. The waves bounce their way through the guide. In the direction of their bouncing path they travel with the wave number $k=k_0$. However, if we look at their propagation down the axis of the guide they propagate with a different wave number $k_z=k_0 \cos\theta$ [28].

Quasioptical interactions within our layer may change the direction of the two uniform planewaves described above. Consider the cross-section of a tilted quasioptical flat mirror within our guiding structure, as depicted in Figure 2.8. The incident TEM-mode radiation depicted at the left of the figure propagates with a wavevector $\mathbf{k_i}$, directed parallel to the guide plates with magnitude $|\mathbf{k_i}|=k_0$. The incident TEM-mode field is:

$$E_i = Ae^{-jk_0\vec{k}_i} \tag{2-15}$$

Radiation strikes the tilted mirror at an angle, θ_i, formed between the mirror normal and the wave vector $\mathbf{k_i}$. Upon reflection from the integrated mirror the reflected radiation propagates in a new direction, $\mathbf{k_r}$, which by the law of reflection points in a direction $2\theta_i$ from $\mathbf{k_i}$. The magnitude of the reflected wave vector remains the same at $2\pi/\lambda$. The projection of $\mathbf{k_r}$, we will call this value $\mathbf{k_{zr}}$, on $\mathbf{k_i}$ is related to the mirror tilt angle θ_i by:

$$k_{zr} = k_0 \cos 2\theta_i \tag{2-16}$$

and the reflected field may be written as:

$$E_r = Ae^{j\left(k_0 \sin\left(2\theta_i\right)y + k_0 \cos\left(2\theta_i\right)z\right)} \tag{2-17}$$

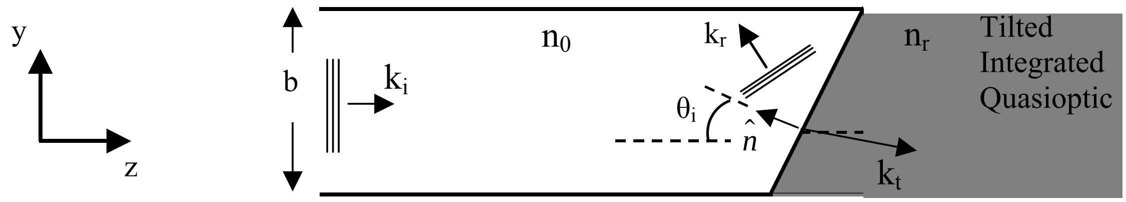

Figure 2.8: Parallel plate guide incorporating an otherwise perfect quasioptical element with a tilted first surface. The tilt of the element is exaggerated for clarity. A TEM-mode field is incident from the left and the reflected and transmitted fields are depicted after interacting with the element surface.

To determine a maximum acceptable angle for mirror tilt, we examine a typical guide and THz-TDS system. The guide is filled with dry air and has a plate spacing, b, of 100 μm. The useful bandwidth of the THz-TDS system extends to 4.5 THz. The first higher-order mode in the guide spectrum is the TM_1-mode. Within this mode the frequency dependence of the z-directed wave number is given as:

$$k_z = \sqrt{\omega^2 \mu\varepsilon - \left(\frac{m\pi}{b}\right)^2} \tag{2-18}$$

We may make a crude approximation to the mirror tilt angle resulting in *maximum* coupling to the TM_1-mode by equating the z-directed phase constants of a single tilted planewave and that of the waveguide mode. In other words, (2-16) is set equal to (2-18), yielding:

$$\cos 2\theta_i = \sqrt{1-\left(\frac{mc}{2fb}\right)^2} \tag{2-19}$$

In this case, θ is the approximate mirror tilt angle for maximum coupling. Therefore, we want any unintentionally fabricated mirror tilt angle to be much less than θ to minimize such coupling. As illustrated by Equation (2-19) and plotted in Figure 2.9, for a given plate spacing, it is the highest frequency of interest that is most sensitive to mirror tilt in terms of coupling to higher-order modes. Evaluating (2-19) at 4.5 THz, we arrive at an allowable mirror tilt of much less than 10 degrees to minimize coupling to the first higher-order propagating mode for a spectrum extending to 4.5 THz. In this case, 10 degrees is the mirror tilt angle resulting in maximum coupling to the TM_1-mode.

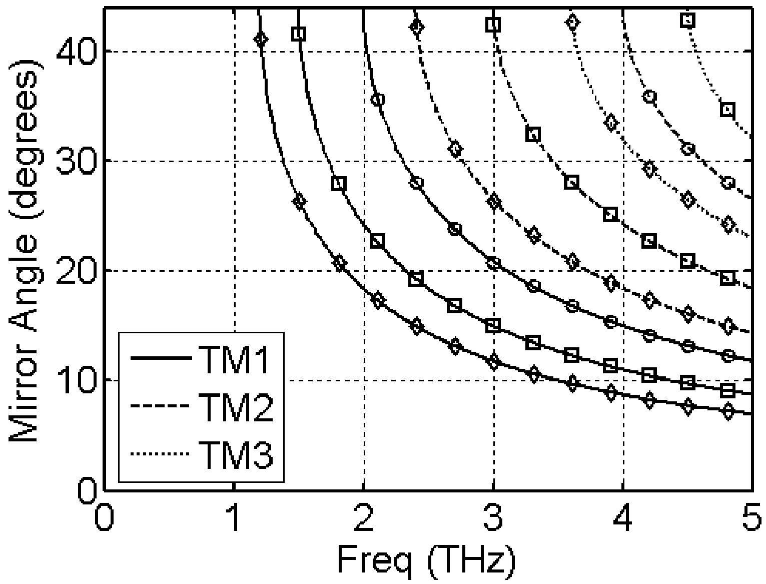

Figure 2.9: Required mirror tilt for maximum coupling of TEM-mode to the indicated higher-order mode for plate spacing of 125 μm (◊), 100 μm (□), and 75 μm (o).

Also evident from Equation (2-19) is that reducing the plate spacing increases the maximum allowable tilt angle by sliding the curves in Figure 2.9 to the right. In fact, if the plate spacing is made less than 33 μm, the excitation of a higher-order propagating mode within our spectrum becomes impossible, which is also evident in Figure 2.3. Simple fabrication techniques may be utilized to fabricate mirrors with a tilt of less than one degree. This fact combines with the fact that, at maximum, we may only couple 50%

of our desired TEM-mode to the next higher mode using a flat mirror with the preceding treatment, allowing the prediction that coupling to higher-order propagating modes by unintentionally tilted mirrors should be minimal. The *magnitude* of higher-order mode coupling is treated in the next two sections.

We now treat transmissive quasioptical elements in an analogous way. Since the reflected power from a transmissive element is generally weaker than the transmitted power, we will be looking at potential mode conversion in the higher-index of refraction lens or prism. In this case we assume that one face of the quasioptical element is tilted and the second face is perfectly perpendicular to the guide plates, in keeping with Figure 2.8. We treat refraction at the lens surface using Snell's law, and arrive at an expression for a lens tilt, again called θ_i, that would result in perfect coupling to the TM_m-mode. After trigonometric substitution we arrive at:

$$\sin(\theta_i) = \left(\frac{k_y}{k_0}\right) \tag{2-20}$$

and it should be stated explicitly again that:

$$k_y = \frac{m\pi}{b} \quad m = 0, 1, 2, \ldots \tag{2-21}$$

This angle is independent of the index of refraction of the lens material (noting the presence of the free space wave number, k_o, in the denominator). As in the case for our tilted mirror we wish to minimize coupling to higher-order modes. Therefore, our lenses must be fabricated with an angularity much less than the calculated value of θ_i. If we again assume a maximum frequency of 4.5 THz and a guide spacing of 100 μm in Equation (2-20), the calculated lens tilt angle should be much less than 20 degrees, which is double that allowed for the reflective case. In fact, it can be shown that for any lens material at any frequency, higher-order mode excitation in a transmissive optic requires twice the tilt of a reflective element. Equation (2-20) may be rewritten as (2-19) with θ_i replaced by $2\theta_i$, and we may simply multiply the curves in Figure 2.9 by a factor of two to obtain a graphical depiction of the transmissive case. Thus, where higher-order mode excitation is expected to be a primary concern, for instance in highly overmoded guides, transmissive elements may be preferred. The next section seeks to predict the magnitude of higher-order mode coupling by a tilted mirror as a function of mirror tilt angle via a simple analytical method. A subsequent section deals with finite-difference time-domain modeling to numerically calculate coupling to higher-order modes due to a tilted mirror.

Higher-order Mode Coupling

In this section we seek a complementary solution to the method above. The goal is to determine the magnitude of higher-order mode coupling from a tilted mirror. The field reflected by a tilted mirror couples to the mode spectrum of the guide over the bandwidth of interest. We may determine the magnitude of this coupling using a common method for beam coupling in quasioptics, the overlap integral:

$$N_m = \frac{\int_0^b \left| E_r E_{TM_m}^* \right|^2 dy}{\int_0^b \left| E_r E_r^* \right| dy \int_0^b \left| E_{TM_m} E_{TM_m}^* \right| dy} \tag{2-22}$$

In order for coupling to occur, the reflected field must overlap in both amplitude and phase with the modal field. After reflecting from the mirror surface we have re-directed the incident plane wave, as in equation (2-16). It should be noted that this redirected plane wave couldn't meet the boundary conditions imposed by the metal plates alone, as this field has non-zero tangential components at the guide plates. However, we will consider equation (2-17) to approximate the field that is present upon reflection for small tilt angles. At small tilt angles, the tangential electric field of the tilted planewave will be negligibly small. The y-polarized field of the TM_1-mode of the guide is given by:

$$E_1 = \hat{y}\frac{-j\beta}{k_y}\cos\left(k_y y\right)e^{-jk_z z} \tag{2-23}$$

Evaluating equation (2-22) with E_{TMm} given by equation (2-23) and E_r given by equation (2-17) with the substitution $k_{yr} = k_0\sin(2\theta_i)$, we arrive at:

$$N_1 = \frac{4k_y k_{yr}^2}{b\pi\left(k_y^2 - k_{yr}^2\right)^2}\left[\cos\left(k_{yr}b\right)+1\right] \tag{2-24}$$

which for small angles reduces to:

$$N_1 = \frac{8k_y k_{yr}^2}{b\pi\left(k_y^2 - k_{yr}^2\right)^2} \tag{2-25}$$

The TM_2-mode may be treated in an analogous way, however such a treatment taken at small angles results in zero coupling, and is thus neglected here. Using equations (2-24,25) we may plot the power coupling efficiency to the TM_1-mode at small angles. This plot is shown as Figure 2.10 below.

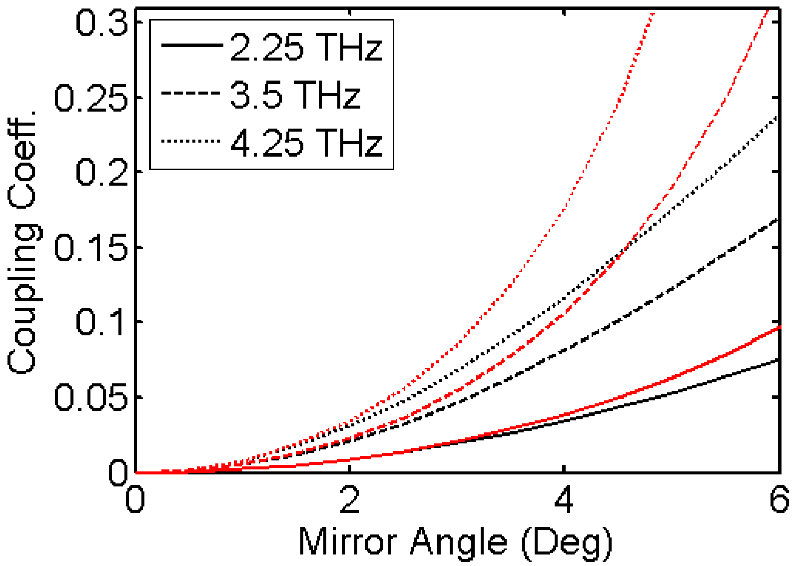

Figure 2.10: Quasioptically determined (black) TM_1-mode coupling coefficients, and the small angle approximation of this method (red).

This treatment suggests that coupling to the TM_1-mode is low for mirrors tilted at very small angles to the guide plates. From the treatment it is again evident that higher-order mode coupling due to a tilted mirror is more severe at higher frequencies. It is also apparent that the magnitude of coupling may become significant even for fairly small tilt angles and/or higher frequencies. However, as this treatment involves the assumption of a reflected field that does not meet the boundary conditions, it is not clear to what extent this approximation is valid. To examine this phenomenon more thoroughly, a finite difference technique has been explored.

FDTD Modeling of a Tilted Mirror

The finite-difference time-domain (FDTD) technique discretizes Maxwell's time-dependent curl equations by approximating the component derivatives as simple difference equations. Detailed summaries of this method may be found in [39-41]. The geometry modeled by this method is shown in Figure 2.11 below:

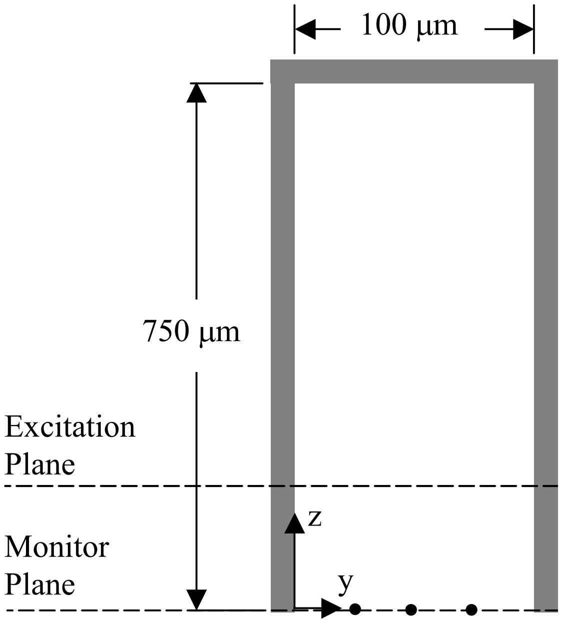

Figure 2.11: Schematic depiction of FDTD solution space for tilted mirror simulation depicting the excitation plane and field monitoring points. Not to scale.

The modeling software used was derived from software accompanying ref [42], which is attributed to [43] in file. This code was extensively modified, with the Berenger perfectly matched anti-reflecting boundary layers and the difference equations retained from the original code. The FDTD calculations are performed using a rectangular grid of square elements with a side length of 0.5 μm, which is λ/66 at 4.5 THz. Numerical stability is insured by operating with a numerical stability (Courant) factor of 0.125 [39, p59], resulting in a time step size of 2.08 x 10^{-16} s. However, operating the simulation with a stability factor of 0.5, which also ensures stability, results in a difference of the calculated coupling coefficients by less than 3% over the entire calculated range, while enabling the calculation to run in 25% of the time of the calculations whose results follow.

In order to examine only propagating modes, we must monitor the field at a sufficient distance from the mirror such that the non-propagating higher-order modes excited by the tilted mirror are highly attenuated. To determine the magnitude of the evanescent fields at the monitor plane, the absorption coefficient is calculated using equation (2-18) below cutoff for the relevant mode. The cutoff TM_1-mode experiences the least attenuation and the amplitude of the excited evanescent waves at the monitor plane is shown as a function of frequency in Figure 2.12 below. This figure illustrates that, except very near the cutoff frequency of 1.5 THz, detection of higher-order evanescent modes at the monitor plane is negligible. Note that contributions from evanescent modes at the monitor plane occur *below* the mode cutoff frequencies.

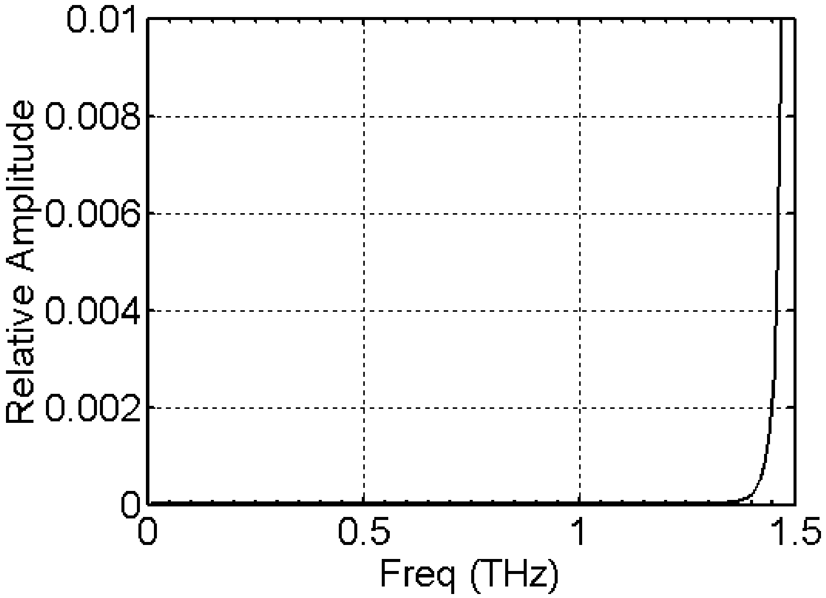

Figure 2.12: Amplitude of the evanescent TM_1-mode at the measurement plane for the FDTD geometry shown above. Note that the vertical scale depicts values ≤1% of the excited field.

As indicated in Figure 2.11, the field is monitored at specific points between the guide plates. Since the amplitude of an excited mode is independent of the y-coordinate except through a known cosine dependence [28, eq. 3.48b], we may choose these points at convenient locations. We consider these locations in light of the fact that only the TEM, TM_1, and TM_2-modes may propagate given a plate spacing of 100 μm and an upper limit of 4.5 THz on our spectrum. At all points along a line of constant z, the amplitude of the TEM-mode is constant. At the point $y=b/2$ the TM_1-mode has zero amplitude, while the TM_2-mode has maximum amplitude. At the points $y=b/4$ and $y=3b/4$ the TM_1-mode is anti-symmetric, with a peak amplitude multiplied by ±0.707. At these points the TM_2-mode has zero amplitude. Thus, by monitoring the field that propagates through these three points, one may determine the amplitude of the fields traveling in each of the three modes by algebraic manipulation of the detected signals. If the field is mapped as a function of time, these amplitudes may be determined for a range of frequencies. For frequencies just above the mode cutoff frequencies, energy travels at a very slow velocity. Due to the necessary finite length of time the field is monitored, the frequencies traveling at these slow velocities may never reach the monitor plane and are not detected. We therefore expect “holes” in our detected spectra *above* the mode cutoffs that are the result of finite temporal sampling.

The total time sample employed in the FDTD technique described here allows for the measurement of signals propagating at velocities as low as ~c/5. From the group velocity dispersion curves shown in Figure 2.13 and the evanescent absorption curve of Figure 2.12 and a similar curve for the TM_2-mode, which is not shown, we may determine a region about each mode cutoff that must be avoided for accurate results to be obtained by post processing of the FDTD derived data. Below cutoff the region to avoid is determined for frequencies where the evanescent field is <0.01% of the reflected value while the upper limit of the excluded region is determined by the slowest frequency component above cutoff arriving in our temporal sampling range. These regions are 1.38 to 1.53 THz and 2.94 to 3.06 THz, for the TM_1 and TM_2-modes. In practice we will stay well away from these regions when comparing mode amplitudes.

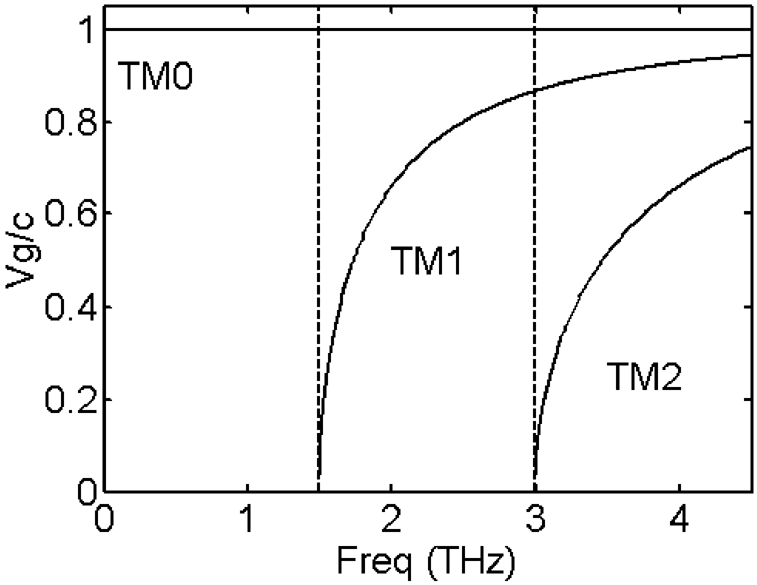

Figure 2.13: Group velocity of radiation traveling in a lossless PPWG with 100 μm plate spacing for the indicated modes. Cutoff frequencies appear as dashed vertical lines.

The amplitudes of the coupled waveguide modes are not conserved, however, power is conserved between the modes in our lossless system. Once the modes are separated in time, as described above, each mode is Fourier transformed with the spectrum converted to (z-directed) power noting the relationship:

$$P_m = \frac{|A_m|^2}{2 \in_n Z_m^{TM}} \tag{2-25}$$

where the A_m are determined from the Fourier transform of the time data, $\in_n$ is Neumann's number ($\in_n$=1 for m=0, $\in_n$=2 otherwise), and Z_m^{TM} is the frequency dependent characteristic impedance of the guide for a given TM-mode which may be calculated as:

$$Z_m^{TM} = \sqrt{\eta_o^2 - \frac{m}{4\pi b f^2 \varepsilon^2}} \tag{2-26}$$

Equation (2-25) illustrates that the power in each of the modes propagates independently from all other modes [46, p337]. Therefore, the power in the individual propagating modes excited by the tilted mirror should sum to yield the power in the excitation pulse. This fact was verified as a check to the FDTD and processing algorithms yielding a variation of <2% for the range of angles from 1 to 7 degrees and <1% for angles 4 degrees and less neglecting the regions near mode cutoffs. Therefore, power-coupling calculations are considered accurate to within this range.

Figure 2.14 depicts the FDTD calculated power coupling out of the TEM-mode to the TM_1-mode over the same range of mirror tilt angles and frequencies as Figure 2.10, which is replotted in red. Note that the calculated values are at frequencies well away from mode cutoffs to avoid the previously described effects.

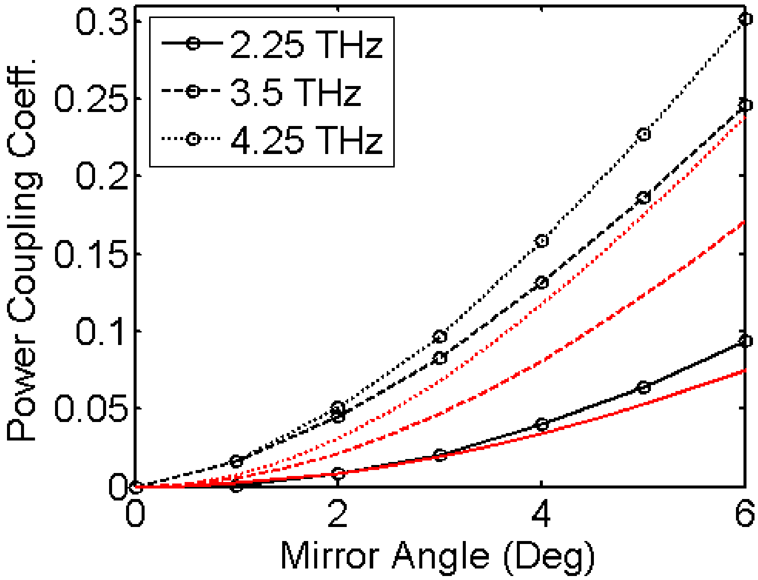

Figure 2.14: FDTD calculated (black) and quasioptically approximated (red) power coupling coefficient to the TM_1-mode at the frequencies indicated. Open circles indicate FDTD calculated data points, while solid black lines are a guide to the eye.

Figure 2.14 is plotted to compare the results of the simple method to treat coupling at small mirror tilt angles developed in the previous section with the FDTD models described above. However, it may be of practical interest to extend the range of Figure 2.14 to consider larger, intentionally fabricated mirror tilt angles and coupling to the TM_2-mode. Figure 2.15 and Figure 2.16 plot power-coupling coefficients to the TM_1 and TM_2-modes for angles up to 25 degrees. For the TM_1-mode both the approximate and FDTD numerical methods yield similar behavior with somewhat varying magnitudes. As mentioned in the previous section, the quasioptical approximation for the TM_2-mode predicts zero coupling at small angles, which is consistent with that shown in Figure 2.16. Finally, for frequencies lying above the TM_2 cutoff there appears to be a mirror tilt angle where coupling shifts from primarily to the TM_1-mode to the TM_2-mode. This observation may have implications for mode converter design in future applications.

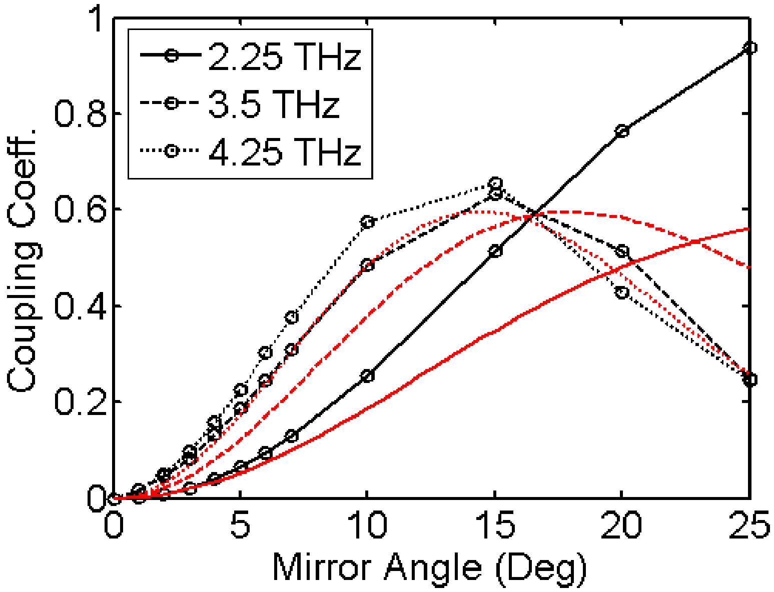

Figure 2.15: FDTD calculated (black) and quasioptically approximated (red) TM_1-mode power coupling coefficients as a function of mirror tilt angle.

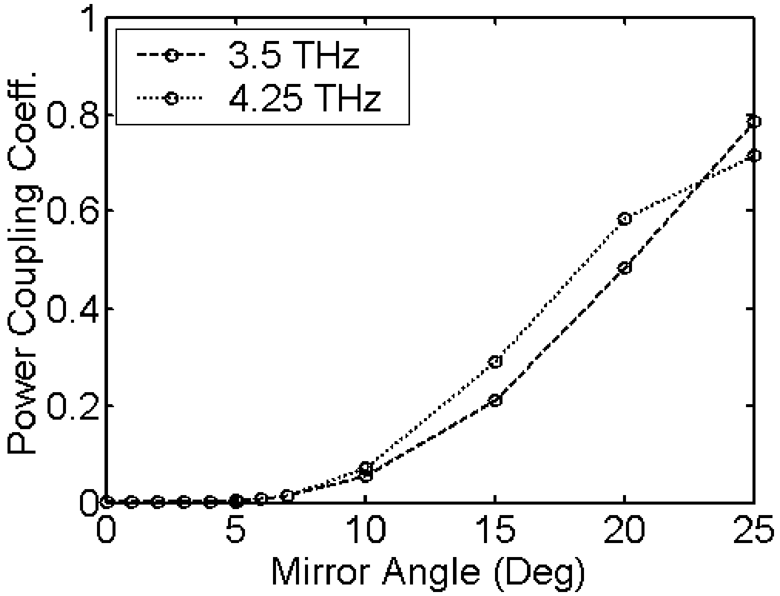

Figure 2.16: FDTD calculated power coupling coefficient to the TM_2 mode at the frequencies and angles indicated. Circles are FDTD calculated data points; lines are a guide to the eye.

The figures above allow comparison among the previously developed methods for treating a tilted mirror. In each case, the quasioptical approximation predicts a lesser magnitude of coupling than the FDTD method. However, the quasioptical method likely *underestimates* the magnitude of the coupling as it completely neglects the tangential components of the electric field introduced by the tilted interface. Despite this omission, at lower frequencies and small tilt angles the method yields very similar results to the more time consuming FDTD calculation. The FDTD calculations likely *overestimate* the coupling coefficient due to the quantization of space, and the necessarily staggered representation of a tilted mirror. This staggered interface likely causes excessive mode conversion when compared to a smooth interface. Thus, the actual coupling coefficient is considered to lie between the black and red lines plotted for the two methods at the indicated frequencies. Note that the form of the curves is similar for both methods.

Finally, if we substitute the frequencies in Figure 2.15 into equation (2-19) we arrive at mirror tilt angles (for maximum coupling) of 21, 13, and 10 degrees for 2.25, 3.5, and 4.25 THz, respectively. If we compare these values to the curves in Figure 2.15 we can see that the actual mirror tilt angle for maximum coupling is somewhat higher in all cases shown than that predicted by equation (2-19). Nevertheless, equation (2-19) provides a quick method for determining a mirror tilt angle resulting in maximum coupling from the TEM to the TM_1-mode. If we divide the angle calculated by equation (2-19) by a factor of ten we have a rule of thumb angle to keep fabrication tolerances below to minimize mode conversion. Subsequent, more time consuming, calculations may be performed to arrive at a more precise angle for maximum coupling as well as determining the amplitude of the coupling for intentionally fabricated tilted mirrors. Thus, all three of the methods presented show utility for determining higher-order mode coupling properties of tilted quasioptical elements in a parallel plate waveguide.

A final note is in order regarding the FDTD simulation. Errors may arise due to the geometric representation of boundary conditions by square elements or a host of numerical effects. The choice of the small 0.5 μm grid size was made to accurately represent the device geometry. However, the FDTD simulation described above was recalculated using smaller grid elements of 0.25 μm for a 5 degree tilted mirror to improve the representation of the actual device geometry. The recalculated coupling coefficients varied by less than 3% of the values shown in Figure 2.15-Figure 2.16. The required calculation time increased from ~8 hours to ~48 hours per calculated tilt angle.

Furthermore, by using the low value of 0.125 for the numerical stability factor in the simulation, numerical dispersion was minimized. The numerically induced variation in phase velocity under these parameters had a magnitude of <<0.02, and no results were cited that required this degree of accuracy for the phase velocity.

The Effect of Incorporated Gaps

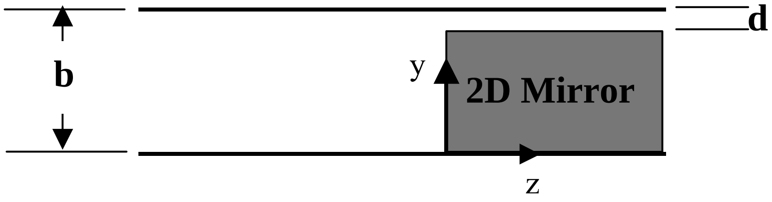

Figure 2.17: Parallel plate waveguide with integrated 2D mirror. The effects of including a gap of width d between the mirror and guide plate are approximated by considering the gap to be a thin section of parallel plate guide.

As our guiding layer may be fabricated from discrete quasioptical elements, we are also interested in the effects of gaps between the plates and optical elements. We may model the unintentional incorporation of a gap between a 2D mirror and the layer plates as a waveguide junction formed by a widely spaced guide to a smaller guide. The cross-section of such a junction is shown in Figure 2.17. The power incident on the reflecting surface is given by the cross-product of the electric and magnetic fields of the TEM-mode, resulting in:

$$P_i = \hat{z}\frac{|A_i|^2 b}{2\eta} \tag{2-27}$$

The magnitude of the electric field transmitted at the discontinuity is given by:

$$|A_t| = \frac{1}{d}\int_0^d E_i(y; z=0)\,dy \tag{2-28}$$

which is also $|A_i|$, as in [44]. The power transmitted in the smaller guide is therefore:

$$P_t = \hat{z}\frac{|A_i|^2 d}{2\eta} \tag{2-29}$$

We may now say that the reflected power from a perfect mirror with an incorporated gap is the difference between the incident power and that transmitted through the gap, which reduces to:

$$P_r = P_i\left(1-\frac{d}{b}\right) \tag{2-30}$$

The mirror loss due to the incorporation of gaps between the mirror and plates is then approximately the ratio of the gap width to the plate spacing.

An alternative way of viewing this problem is as a junction between two transmission lines, as depicted in Figure 2.18. The step discontinuity affects only the electric field of the input excitation, resulting in TM-mode coupling between the two guides. For simplicity we assume that the plate spacing and bandwidth of interest is chosen such that only the dominant TEM-mode may propagate in each guide. As the electric field is continuous across the boundary, the discontinuity is equivalent to a shunt capacitive susceptance, jB. The equivalent transmission line circuit is depicted in Figure 2.18. Collin has calculated first-order and corrected approximations to the value of this susceptance [46, p600, prob. 8.2]. However, the result of this treatment is that the susceptance is linear in frequency, resulting in a linearly frequency dependent phase shift for all frequencies for the reflected pulse. Thus, the reflected pulse is simply a time-shifted version of the incident wave whose magnitude has been reduced by some factor.

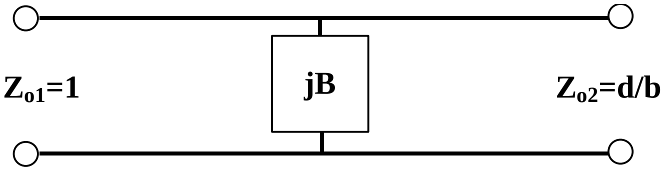

Figure 2.18: Equivalent transmission line circuit for PPWG incorporating a small gap between the guide plate and mirror surface.

Using the equivalent transmission line above with the formulas obtained in the reference, we may determine the reflective properties of the junction via standard transmission line techniques. Assuming a gap width of d=3 μm and terminating the second line with a matched load, we arrive at a frequency independent reflection coefficient with a magnitude of 0.94 in amplitude, or ~89% in power. This method predicts such a mirror to be 8% less reflective than that predicted by equation (2-30). The phase shift associated with this reflection is frequency independent at -180 degrees. While both of these methods are approximate, they do give us insight into the nature of reflection from 2D mirror with a small gap between the element and plates. In particular, that the effects are expected to be frequency independent, attenuating the reflected pulse a factor on the order of the ratio of the gap width to plate spacing. As will be shown in a subsequent treatment, realistic gaps, on the order of a few microns between the mirrors and plates, are predicted to be significantly higher sources of loss than the finite conductivity of the metal mirrors and guide plates. In practice, gaps between the mirrors and guide plates appear to be the most critical fabrication concern.

Minimum Quasioptic Size

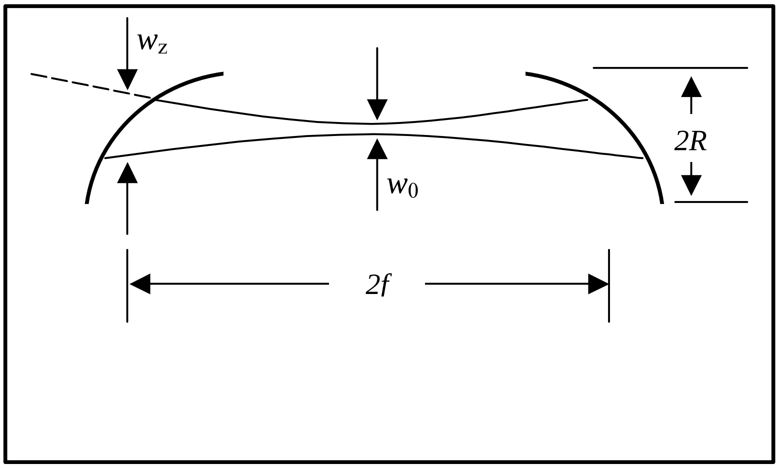

Figure 2.19: 2D TEM-mode integrated optical structure consisting of two confocal parabolic mirrors. A minimum beam waist w_0 is present between the elements, the spot size at a distance from the minimum waist is w_z (shown at the mirror location), the elements are spaced by twice the focal length *f*, and the mirror clear aperture radius is R.

In order to maximize the efficiency of point-to-point coupling we would like to design a 2D quasioptical system such that the beam at all points within the system is smaller than the smallest aperture in the system. We now briefly consider our 2D structures in the context of Gaussian beam theory. As with conventional quasioptical systems, our integrated system must be made of confocal quasioptical elements in order to function with minimum frequency dependence. Confocality of the quasioptical elements requires that a beam waist (radius), w_0, be present at the midpoint between any two focusing optics. We may determine the constraints on quasioptic transverse extent as in Ref. [34] by rearranging equation (2.32b) in Ref. [33] for this special case and simplifying by completing the square,

$$w_0^2 = \frac{1}{2} w_z{}^2 \pm \sqrt{\frac{1}{4} w_z{}^4 - \left(\frac{\lambda f}{\pi}\right)^2} \tag{2-31}$$

where w_0 is the minimum beam waist (1/e half-width), *f* is the focal length of the optic and w_z is the beam waist at a distance from the minimum waist, presumed to be the aperture location. Our aperture radius should be chosen to minimize diffraction, and we can arbitrarily set its value. We will set its value to $R = 3w_z$. In this case, the radius of the lens/mirror clear aperture is three times that of the 1/e beam waist, and the magnitude of the incident field at the aperture is <0.01% of the peak field. Now, in order for w_o to have real solutions with this value of R substituted into Equation (2-31),

$$R \geq 3\sqrt{\frac{2\lambda f}{\pi}}\,, \tag{2-32}$$

which defines either the minimum quasioptic clear aperture half-width, R, in terms of λ and *f*, or focal length given λ and R. Furthermore, we can say that there is a wavelength associated with these two optics corresponding to the maximum wavelength (lowest frequency) still allowing a real value for w_0 in (2-31). This wavelength is given by,

$$\lambda_{diff} = \frac{R^2\pi}{18f}\,. \tag{2-33}$$

We will call this wavelength a "diffraction wavelength." It represents a wavelength longer than which losses due to aperturing effects are expected. The physical size of integrated quasioptics are therefore limited by other parameters of the system. Equation (2-32) allows us to determine the transverse extent of our quasioptics given that we can supply a diffraction wavelength and focal length. We can see from this equation that there are only two ways to reduce the transverse extent of the incorporated quasioptics without introducing excess losses: to place the optics more closely together necessitating the use of shorter focal length optics, or by lowering the diffraction wavelength. Figure 2.20 illustrates the dependence of the aperture width (2R) on both frequency and focal length. From these plots of (2-32) it is clear that diffraction frequency and focal length are competing processes for minimizing the optical aperture width. From the figure it is also clear that for quasioptical elements not to suffer significant effects due to diffraction, their size must be on the order of several millimeters.

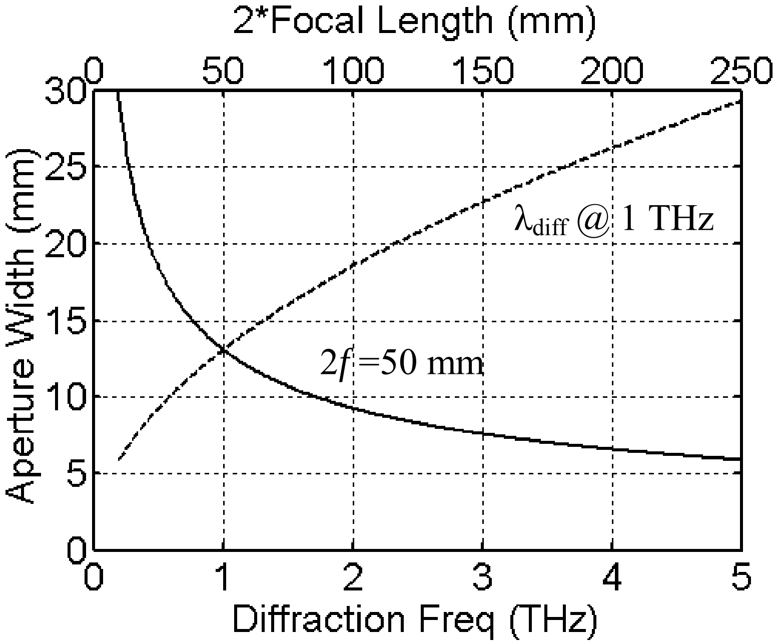

Figure 2.20: Minimum aperture full width: vs cutoff frequency for 2f=50 mm (solid line, lower axis) and vs 2f (dashed line, upper axis) for λ_{diff} @ 1 THz. The aperture width must lie on or above on of these curves.

Summary

This chapter has proposed several design considerations for the development of a planar THz bandwidth guiding structure incorporating two-dimensional quasioptical elements. The layer supports TEM-mode propagation, unlike all other platforms for integrated (quasi)optics. In this mode, standard quasioptical techniques may be used to analyze the propagating radiation and quasioptical interactions within the structure. This fact is the result of the elimination of the quantized k_y component of the wave vector by considering the TEM-mode. The practical concerns affecting plate spacing, angularity of incorporated quasioptical elements, the effect of gaps, and the transverse extent of the elements have been considered. A set of design curves and equations were generated to facilitate rapid 2D quasioptical system design relating plate spacing, absorption loss, and dispersion. Together these considerations form a new preliminary set of tools for the development of planar quasioptical systems. The graphs and equations of this chapter may be used to quickly determine the required geometries for approximate system performance. Chapter 3 experimentally demonstrates and examines several 2D quasioptical elements.

Chapter 3

Demonstration of 2D TEM-mode Quasioptics

In this chapter two-dimensional quasioptical elements are demonstrated within an ultrahigh bandwidth TEM-mode guiding structure in the THz regime. The so-called THz interconnect layer guides sub-ps THz bandwidth pulses in both dimensions transverse to the direction of propagation. It does so by incorporating 2D quasioptical elements within a sub-wavelength spaced parallel metal plate structure. While the concept is similar to other integrated optical techniques, the TEM-mode guiding structure demonstrated here exhibits negligible dispersion, ease of fabrication, low-loss, and easy maintenance of the TEM-guided mode. These features make the layer quantitatively unique from other integrated optical guiding structures, as demonstrated in the previous chapter. By incorporating optical elements within a TEM-mode guiding structure, the THz interconnect layer forms a configurable THz bandwidth TEM-mode planar interconnect with low loss and negligible GVD. The layer also exhibits the unique potential to be directly optoelectronically excited by the PPT transmitter described in subsequent chapters. The direct excitation of the layer is a key step for point-to-point communication utilizing the structure to be realized. Portions of the data and theory contained in this chapter have been previously published [48,49].

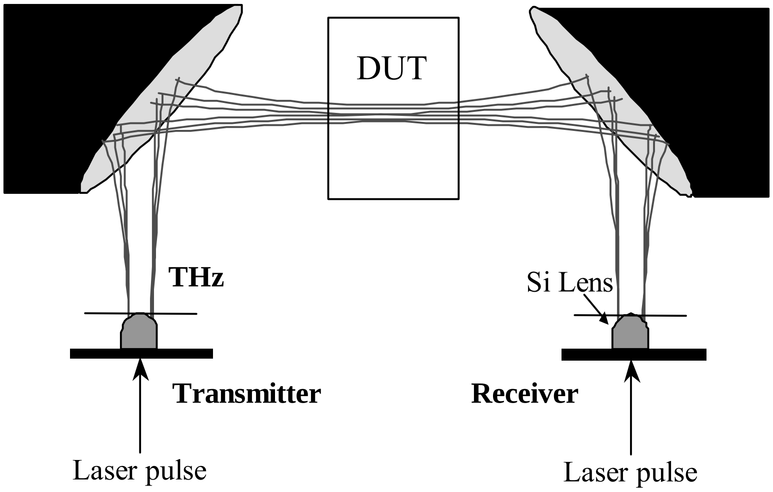

Figure 3.1: Standard THz-TDS arrangement with device under test (DUT) placed at the confocal beam waist between two off-axis parabolic mirrors.

As described by Gallot and Grischkowsky for previous THz waveguide studies, excitation for the THz interconnect layer was provided by quasioptically coupling to a beam of freely propagating THz radiation in a standard THz-TDS arrangement [6]. The specific test arrangement is described in Figure 3.1. The interconnect layer is placed in the confocal beam waist between two off-axis parabolic mirrors. In the absence of an interconnect layer the beam waist at this location is linearly frequency dependent, with a waist diameter of approximately 9 mm at 1 THz.

Layer Fabrication

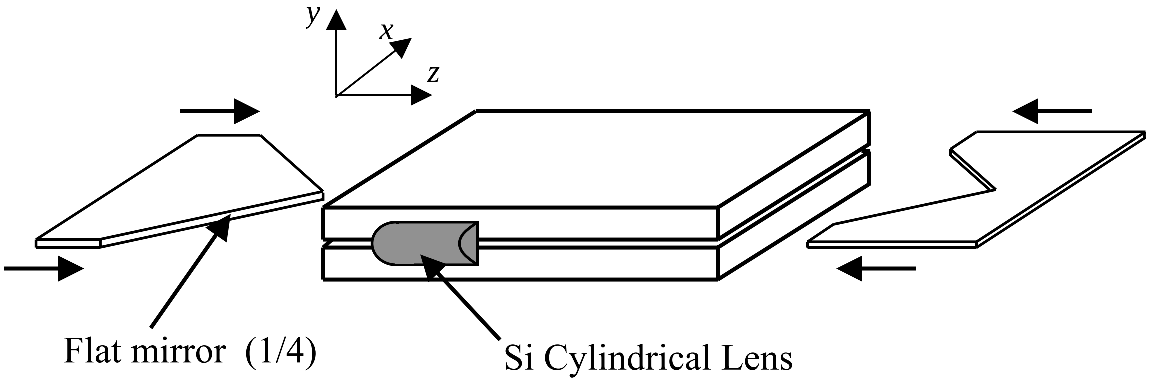

Figure 3.2: Exploded isometric drawing of PPWG incorporating four quasioptical flat mirrors (not to scale).

The investigated interconnect consists of two relatively large (many cm) metal plates separated from each other by 100 μm. This plate spacing was chosen as a compromise for low-loss operation as shown by Figure 2.4, a low number of propagating modes in the available bandwidth as shown by Figure 2.3, low dispersion as shown by Figure 2.5, and ease of fabrication. Within this 100 μm-thick, dry-air filled layer, planar quasioptical components may be placed to guide, collimate, focus, or diffract the propagating THz TEM waves. The simplest possible intra-guide quasioptical component is a flat mirror. In order to simplify the experimental arrangement as much as possible, and to determine the effects of incorporating quasioptical elements within a sub-wavelength structure, the first demonstration of the layer was made using four intra-guide flat mirrors. The investigated geometry is illustrated in Figure 3.2.

For this experiment two externally identical parallel plate interconnects were fabricated from 9.5 mm thick oxygen free Copper alloy 101 plate, machined to shape and polished by hand. The external dimensions of each structure were 100 mm in the *z*-direction, 76 mm in the *x*-direction, with a 19 mm overall height in the *y*-direction. Both structures used 100 μm thick Copper alloy 110 shim stock to maintain the plate spacing, and the same material was used for the integrated mirrors. As the layer is only 100 μm thick, it is the edges of the shim stock that are used as the reflecting surfaces of the integrated quasioptical elements. These mirrors were hand polished such that the edges remained square with sharp corners and flat reflecting surfaces. This was done by careful fabrication using specially designed polishing jigs specific to each set of mirrors. These jigs helped to minimize any y-dependence for a given mirror, thereby minimizing the potential for higher-order mode excitation. Device final cleaning and assembly was performed in a cleanroom in order to minimize the incorporation of dust and contaminants between the layer plates and the mirrors/shims.

Two interconnect structures were fabricated to facilitate measurement of the layer absorption. The first interconnect incorporated no internal quasioptical elements and had a straight through path length of 68 mm, depicted as path-1 in Figure 3.3. This structure therefore functioned as a standard parallel-plate waveguide. The second interconnect had a 146 mm guided path length, achieved by making four reflections from planar quasioptical flat mirrors incorporated within the layer, illustrated as path-2 in Figure 3.3, and depicted in the isometric drawing of Figure 3.2. Because the two interconnect structures were externally identical, the positions of their included silicon lenses relative to the confocal beam waist of the THZ-TDS system did not change with the internal THz path length.

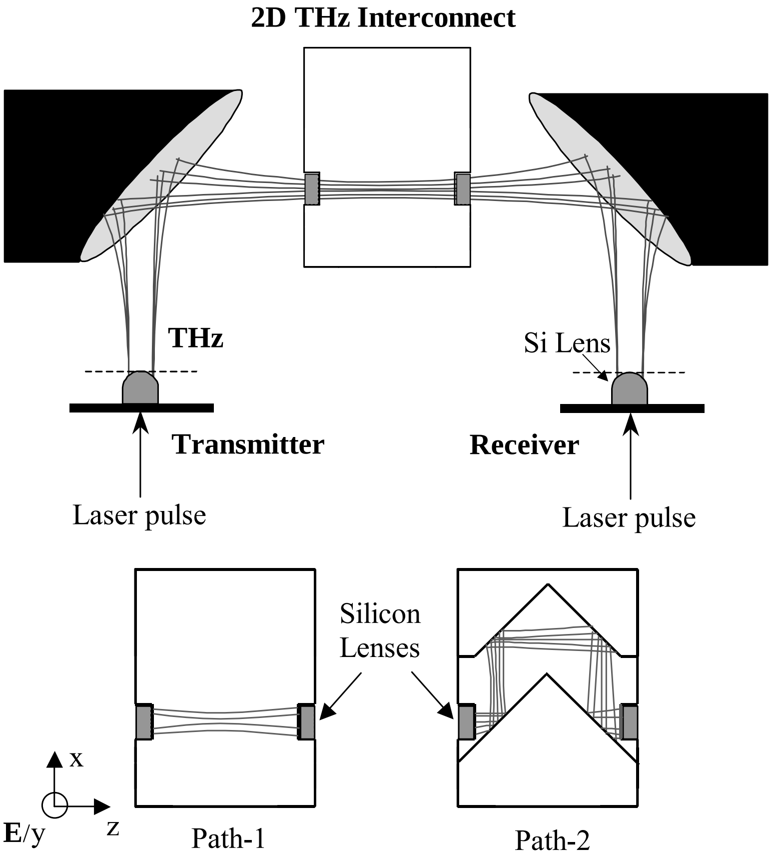

Figure 3.3: THz-TDS arrangement for determining the loss of the parallel plate structure incorporating four reflections to a standard parallel plate guide. Path-1 illustrates the 68 mm straight path and Path-2 illustrates the 146 mm reflective path.

The interconnect layer, as fabricated above, was placed in the standard confocal THz-TDS arrangement [10]. Inserting the interconnect layer also inserts two high-resistivity silicon cylindrical lenses into the beam path. These lenses are 15 mm in the x-direction, 10 mm in the y-direction, and have a thickness of 6.56 mm with a radius of curvature of 5 mm. The 6.56 mm lens height has empirically been determined to exhibit the best quasioptical coupling to the interconnect layer of available silicon lenses. The planar portion of the lens was placed in contact with the interconnect structure. At the foci of these lenses, the THz beam forms an elliptical spot. The spot has a frequency independent minor axis with an approximate length of 200 μm and a frequency dependent major axis with a length of 9 mm at 1 THz. The phase front presented to the interconnect layer is assumed to be planar, with a polarization normal to the layer plates. The amplitude profile of the beam is essentially uniform in the *y*-direction over the spacing of the guide plates, and can be described as a Hermite-Gaussian in the *x*-direction.

The experimental investigation of the layer began by taking a reference pulse with no interconnect or silicon lenses placed in the THz-TDS system. The 68 mm long straight interconnect was then placed at the confocal THz beam waist with the cylindrical lenses attached. The cylindrical lenses were adjusted to obtain a peak time domain signal and several scans were taken. Multiple scans were taken to ensure system stability and provide for noise reduction via averaging should it be necessary in post processing of the data. The interconnect was removed and minor adjustments were made to the system to maximize the signal again. The 146 mm interconnect layer incorporating four reflections from 2D flat mirrors was then inserted at the confocal THz beam waist. The cylindrical lenses were again adjusted to obtain a maximum peak signal and several scans were subsequently taken. After interconnect removal, reference scans were again taken in order to estimate the overall system stability. This process was developed and carefully followed in order to assure maximum repeatability for the measured data. No alternate methods were found that insured repeatability. The data displayed in Figure 3.4

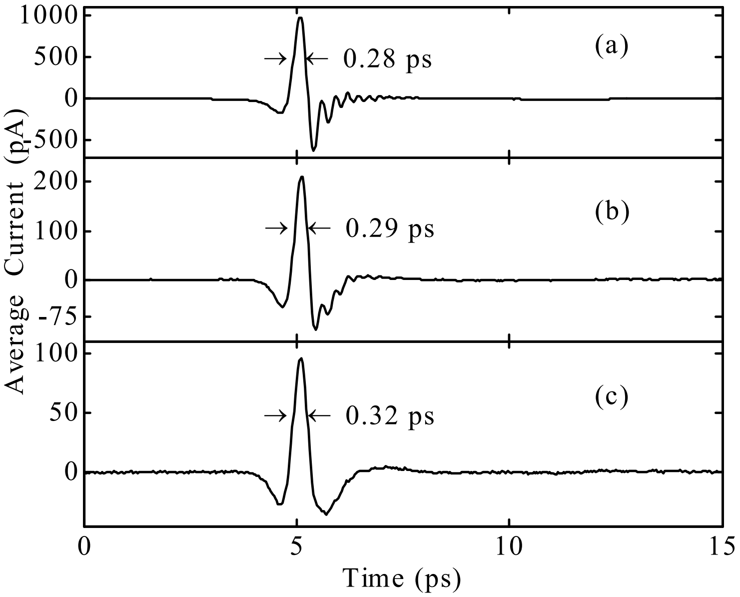

Figure 3.4: THz pulses for (a) the standard THz-TDS arrangement with no interconnect or lenses, (b) the 68 mm straight path, and (c) the 146 mm reflective path. FWHM pulsewidths of the main peaks are indicated by arrows.

is taken from a single scan in each instance. However, each of these experiments was repeated on three separate occasions to ensure reliability of the data. The agreement between each of the three experiments is excellent.

By comparison of the time-domain data in Figure 3.4, we can see that the full-width at half-maximum (FWHM) pulse width of the main signal peak is broadened by only 40 fs after 146 mm propagation through the interconnect layer including four bounces from quasioptical flat mirrors. However, quoting the pulse broadening using FWHM in this way is somewhat misleading. From pulse (a) in Figure 3.4 we can see that there is pronounced temporal ringing in the measured THz field. This ringing is due to dispersion in the GaAs transmitter die, which results in the pulse being positively chirped. That is, the higher frequencies are arriving later in time than the lower frequency components comprising the main peak. It is evident from the pulses in (b) and (c) that the higher frequencies, that is those portions of the pulse arriving later in time, are experiencing a proportionally higher loss than the lower frequencies. This phenomenon is particularly evident in the scaled spectra of Figure 3.5. This loss is due to the frequency dependent absorption of the interconnect layer which is described below. While describing the pulse broadening in terms of that observed for the main peak is potentially misleading, it is the standard method used in the literature and will be used throughout this document.

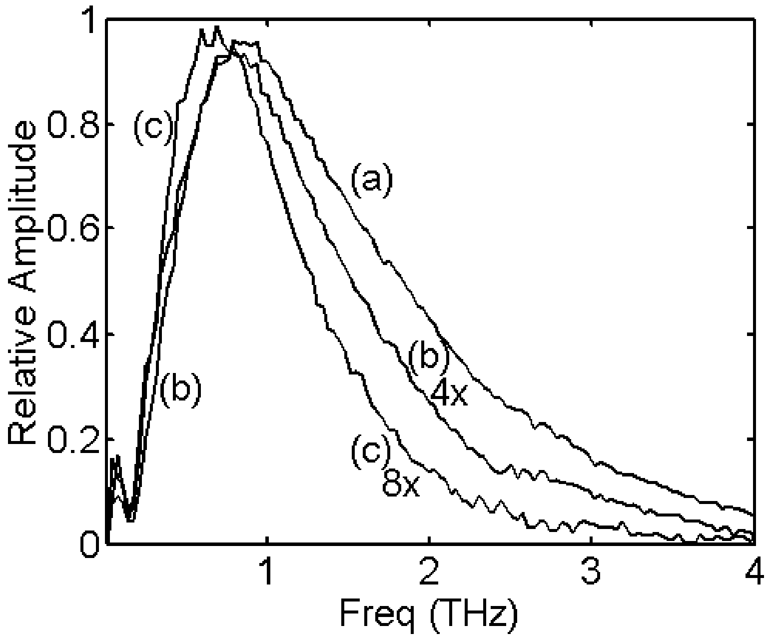

Figure 3.5: Scaled amplitude spectra corresponding to the time domain scans in Figure 3.4(a-c). The scaling factors are indicated in the figure.

Layer Absorption

The absorption of the interconnect layer may be determined by standard linear system analysis. The transfer function of the TEM-mode of the interconnect layer can be written in the temporal frequency domain as:

$$E_{out}(\omega) = E_{ref}(\omega) T C_x {C_y}^2 R^4 e^{-j(k_z L - k_0 d)} e^{-\alpha L} \tag{3-1}$$

where $E_{out}(\omega)$ and $E_{ref}(\omega)$ are the complex spectral components at angular frequency ω for the output (measured) and reference electric fields respectively, T is the amplitude transmission coefficient accounting for the Fresnel reflections from the cylindrical lens surfaces, C_x is the coupling coefficient in the *x*-direction which is assumed to be 100% at the input and therefore is not squared. C_y is the coupling coefficient in the *y*-direction. R is the amplitude reflectivity of the individual 2D interconnect mirrors, set to unity for the straight path. L is the guided wave path length in the interconnect and d is the corresponding free space path length with the interconnect removed. α is the layer amplitude attenuation constant, k_z is the phase constant and $k_0 = (2\pi/\lambda)$, where λ is the free space wavelength.

Applying Eq. (3-1) to the straight path (path-1) and reflective path (path-2) data separately and taking the absolute value of their complex ratio, we obtain an expression for an effective amplitude absorption coefficient, α_{eff}, that depends on the ratio of the measured electric fields, which include the effect of the coupling in the *x*-direction and the reflectivity of the four mirrors:

$$\alpha_{eff} = \frac{1}{(L_1 - L_2)} \ln \left| \frac{E_{out2}}{E_{out1}} \right| . \tag{3-2}$$

where L_1 corresponds to path-1 (68 mm) and L_2 corresponds to path-2 (146 mm). The measured effective absorption from Equation (3-2) is shown as open circles in Figure 3.6. The data used is the average of data taken from three separate experiments. The measured effective absorption may be compared to that expected for the TEM-mode of a parallel plate waveguide with no internal quasioptical elements. The theoretical absorption coefficient for the TEM-mode of an air filled parallel plate waveguide is,

$$\alpha = \frac{\left(10.88x10^{-3} \left[\frac{10^7}{\sigma \lambda_0} \right]^{0.5} \right)}{\eta_0 b} \quad \text{[ref. 45]} \tag{3-3}$$

where η_0 is the wave impedance of free space ($\eta_0 = (\mu_0/\varepsilon_0)^{1/2} \sim 377\ \Omega$), b is the plate separation (100 μm), and σ is the conductivity of copper ($5.8x10^7\ \Omega^{-1}m^{-1}$). The theoretical absorption of (3-3) for a parallel plate waveguide is plotted as a solid line in Figure 3.6 for comparison. The measured effective absorption coefficient is in reasonable agreement with previous parallel plate waveguide data, even though it includes the four reflections and the C_x coupling losses due to the non-confocality of the system with the interconnect layer installed. The smoothness of the curve indicates negligible loss due to mode conversion. When this data is compared to that obtained for long lengths of PPWG in [11], we consider the reflectivity of the incorporated mirrors to approach unity, thereby confirming the efficacy of our TEM-mode integrated quasioptical approach.

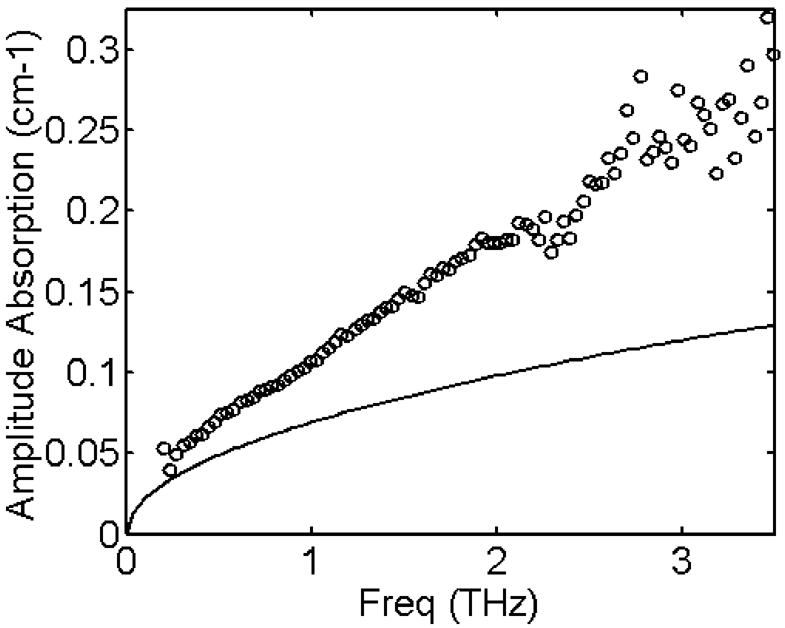

Figure 3.6: Measured absorption spectrum of the interconnect layer incorporating four reflections with no correction for spreading along the *x*-axis.

Compared to the minimum loss of the parallel-plate waveguide as calculated from (3-3), the measured excess loss can be attributed to several potential mechanisms: First, the coupling coefficient C_x was not removed from the measured data. In previous experiments the transmitter and receiver sensitivity patterns were considered to be identical, and the C_x coupling coefficient was calculated based on standard Gaussian beam mode theory. Under this assumption, we plot the corrected curve as Figure 3.7 below. This figure may be compared to the absorption spectrum published in [11]. It should be noted that the guide in the referenced work was 10 percent thinner than the guide demonstrated above and its absorption should therefore be higher.

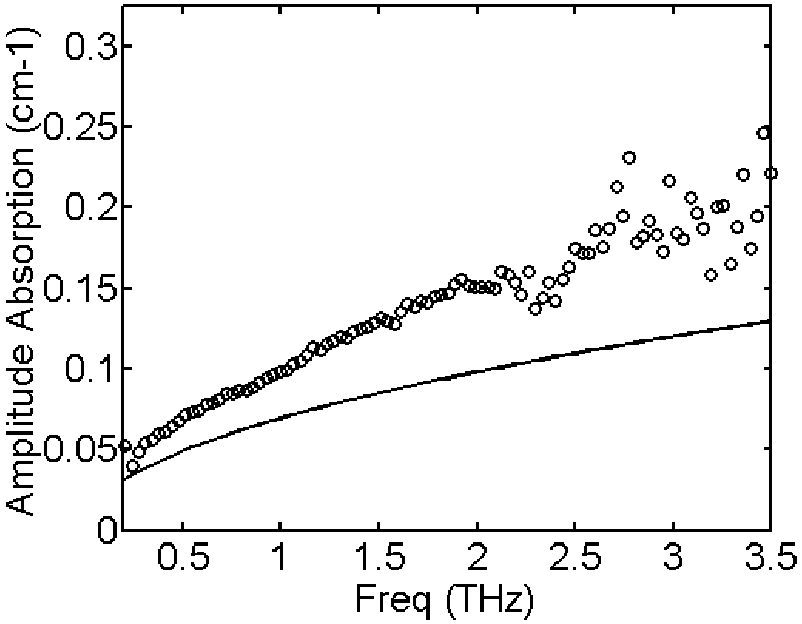

Figure 3.7: Measured absorption spectrum for the reflective interconnect corrected for spreading along the *x*-axis.

A second source of excess loss could be due to the fabrication of the interconnect layer. Some loss is expected as the structure likely has gaps of several microns between the plates and the mirror edges, allowing leakage of the guided mode, as described in Chapter 2. However, significant efforts were made to reduce this effect. As a possible third source of excess loss, the skin depth of copper at the frequencies of interest is approximately 100 nm. Scratches and pits in the layer plates that are significant when compared to the skin depth may lead to an additional frequency dependent loss.

While previously neglected, we will briefly consider the reflectivity of the copper mirrors used within the layer. In this case the plane of incidence of the quasioptical element is parallel to the plane of the layer plates, with the polarization perpendicular to this plane. It is assumed here that the reflectivity of the incorporated mirrors is the same as that in free space. For good conductors, we may assume that the permittivity of a metal is purely imaginary and is given by the equation

$$\varepsilon_m = -j\frac{1.8\times10^9}{f_{GHz}\rho} \tag{3-4}$$

where f_{GHz} is the frequency of interest in GHz, and ρ is the resistivity of the metal used in units of 10^{-8} Ωm, taken as 1.72. We may determine the reflectivity of the mirror using the above equation in:

$$r_{perp} = \frac{\left(\varepsilon_m - \sin^2\theta_i\right)^{0.5} - \cos\theta_i}{\left(\varepsilon_m - \sin^2\theta_i\right)^{0.5} + \cos\theta_i} \tag{3-5}$$

where θ_i is the angle of incidence of the impinging THz beam [33]. In this case, the angle of incidence is taken as 45 degrees. The calculated amplitude reflectance spectrum under these conditions is presented in Figure 3.8. Note that as θ_i is increased to 90 degrees the reflectivity of the mirror goes to 100%.

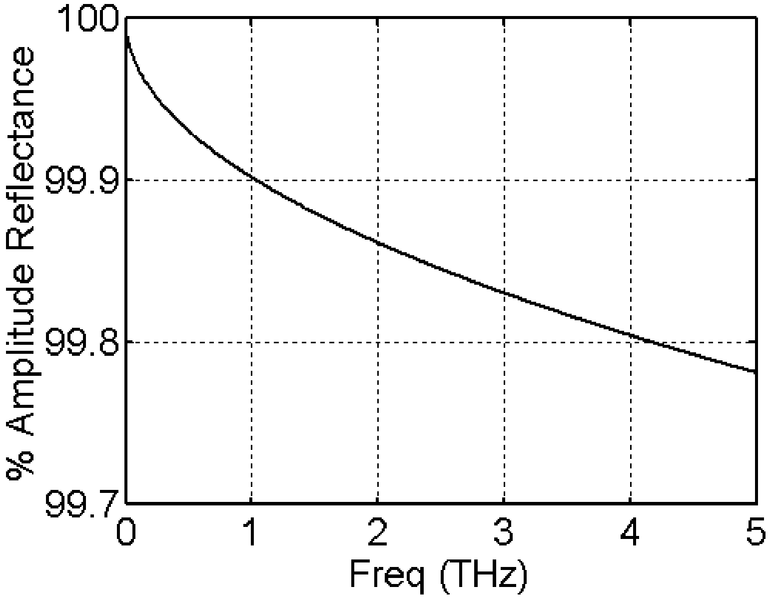

Figure 3.8: Calculated reflectance spectrum of a polished oxygen free copper surface with a 45 degree angle of incidence.

The figure illustrates that the loss from a single reflection at the frequencies of interest is negligible when compared to the absorption of even a short length of guide or that predicted for a gap between the mirror and plates on the order of 1 μm. However, the reflectivity of the mirrors will require further consideration for systems incorporating numerous reflections. Considering that the absorption data measured above includes 4 reflections at 45 degrees, the measured data of Figure 3.7 is essentially unaffected. However, if the correction for mirror reflectivity were made, the corrected loss would more closely resemble the theoretical prediction.

A possible fifth source of excess loss is due to the conductivity of metals at the frequencies of interest. It is mentioned in the literature that metals at these frequencies are often measured to be several times more resistive than at DC [33]. As it was the DC value of resistivity used to determine absorption, this phenomenon could be a primary source of discrepancy between the predicted and measured values.

Integrated Focusing Mirror

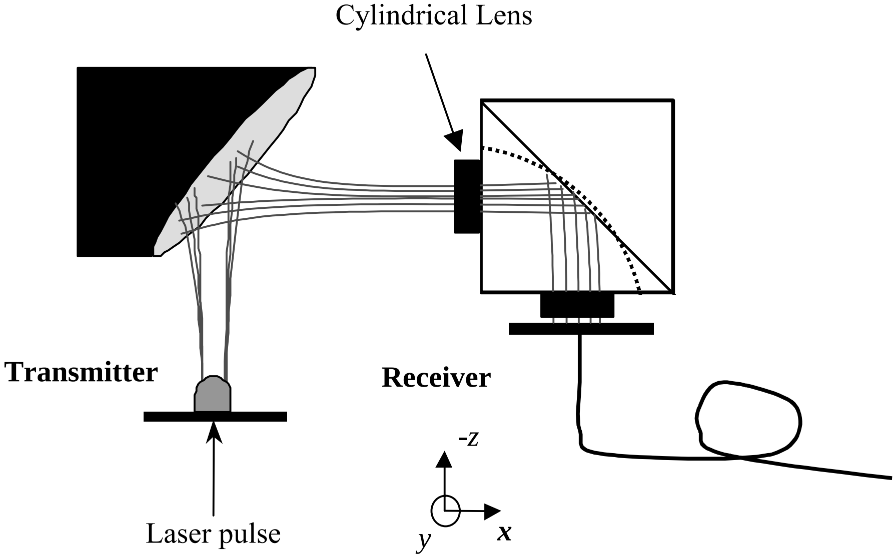

Figure 3.9: Scanning THz system utilizing a fiber-coupled bare-die receiver for mapping the focusing action of a 2D circular mirror. Diagram is not to scale.

This section demonstrates a planar circular reflective quasioptical focusing element incorporated within the interconnect layer. This element is expected to act as a thin lens for the guided radiation in the layer. The experimental arrangement used here is not the typical confocal THz-TDS arrangement used from previous demonstrations. Instead, a technique demonstrated by Reiten *et al.* to map a THz beam using an optical fiber-coupled THz receiver is used [50].

The experimental arrangement used to measure the focusing action of the integrated circular mirror is depicted in Figure 3.9. The receiver may be translated in the *xy*-plane without changing the relative timing of the system, thereby mapping the spatial variation of the output electric field. The demonstrated 2D reflective optics are placed in a parallel plate copper structure measuring 56 mm x 56 mm x 19 mm overall height. The THz beam is coupled into and out of the parallel plate structure by 6.56 mm height silicon cylindrical lenses identical to those used in previous experiments. The reflective elements are fabricated from the same 100 μm thick copper alloy 110 shim stock as in the previous case. Two identical test structures were fabricated, each containing a different 2D integrated quasioptical element. The first, or reference, element was simply a flat reflector angled at 45 degrees to the input beam. The second element was a circular mirror with a radius of 100 mm. A circular geometry was used for simplicity in fabrication of a polishing jig of the same shape. The two configurations are depicted simultaneously in Figure 3.9 although only one element was used per experiment. Ray tracing shows that the focus of the circular mirror lies near the output surface of the output cylindrical lens. Figure 3.10 below depicts the ray-tracing of the circular mirror for a collimated beam with an input waist corresponding to the calculated beam waist at 1 THz. Refraction at the silicon lens surfaces is not considered.

With either test structure in place, the receiver was translated along a line containing the output aperture of the structure to determine the electric field amplitude at the device output. The measurement line lay approximately 5 mm from the output silicon lens face. A reference scan was obtained by placing the test structure containing the flat reflector in the beam. The spatiotemporal relationship of the field was obtained by taking a time-domain scan of the electric field for each increment of receiver translation along the *x*-axis. The measured data is shown in the left panel of Figure 3.11. Data was

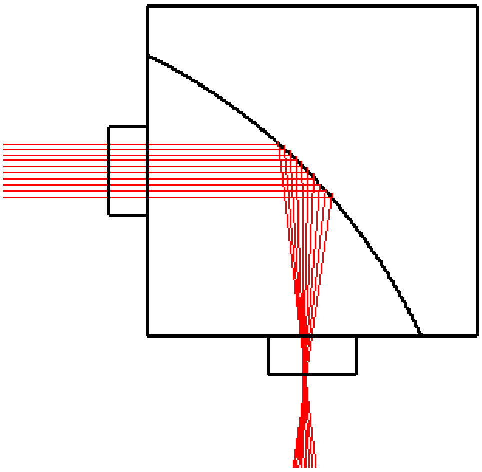

Figure 3.10: Overall focusing mirror test structure depicting the transverse extent of the guiding structure, silicon cylindrical lenses, and 2D focusing mirror. Ray tracing is shown to determine the location of the output focal spot. The test structure geometry is 56 mm square.

recorded for only half of the actual spatial field dependence along the *x*-axis due to the large size of the output beam. To obtain the overall beam profile shown in the figure, the image was reflected about the beam center. Thus, we have made the inherent assumption that the beam profile is symmetric along this axis. This assumption should be valid for the simple flat reflecting surface considered. The focusing action of the circular mirror was then measured in a similar manner and the measured results are shown in the right panel of Figure 3.11. In this case the data shown is the entire measurement with no assumptions regarding symmetry. The two scales are one to one only in time. Note that the extent of the distance axis for the circular mirror is compressed to half that of the reference pulse.

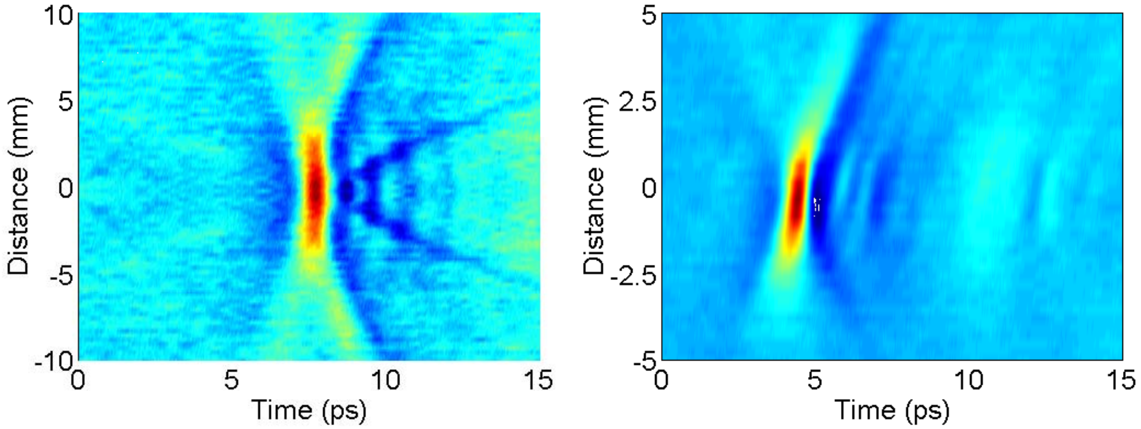

Figure 3.11: Measured spatio-temporal field patterns for the 45 degree flat mirror (left) and circular focusing mirror (right). Due to spatial sampling limits the beam pattern from the flat mirror has been reflected about the line y=0 mm.

The 1/e measured beam diameters for each pulse may be obtained from the figures above. It should be noted that this measurement is not made at a single frequency, but for the entire sampled field. The measured diameters are 7.3 mm for the flat mirror and 3.0 mm for the circular mirror. These measurements clearly show the spatial compression of the field, resulting in an image with an increased signal to noise ratio. We may also determine the FWHM pulsewidth at the center of each beam for both configurations. The measured FWHM pulsewidths are 720 fs for the unfocused case and 540 fs for the focused case. The individual pulses, corresponding to the center of each beam, are shown in Figure 3.12 normalized to their own maxima and offset from one another for clarity. The measured pulsewidths are significantly longer than those in previous measurements due to the use of the fiber coupled receiver without an attached silicon lens.

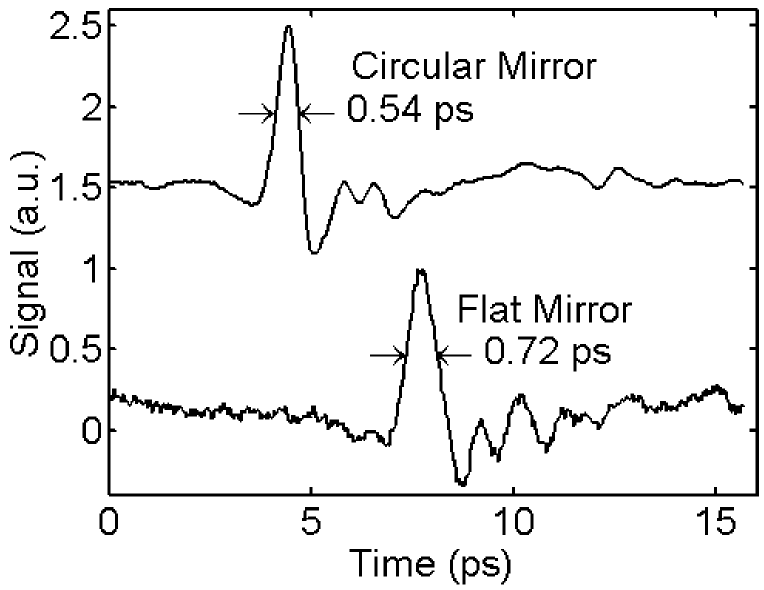

Figure 3.12: Temporal scan along the beam centers illustrating the increased signal-to-noise and decreased pulsewidth of the THz beam when focused by the circular mirror. The flat mirror curve is multiplied by 5.

Analyzing the spatiotemporal data above by performing a discrete Fourier transform on the time-domain portion of the data, we may examine the spatial dependence of the field at specific frequencies. The measured beam profiles at various frequencies for the flat and circular mirrors are depicted in Figure 3.13. The measured 1/e waist diameters for the circular mirror are 3.44, 2.55, 1.81, and 2.19 mm at 0.51, 0.76, 1.0, and 1.28 THz respectively. These measured values may be compared to those expected by theory.

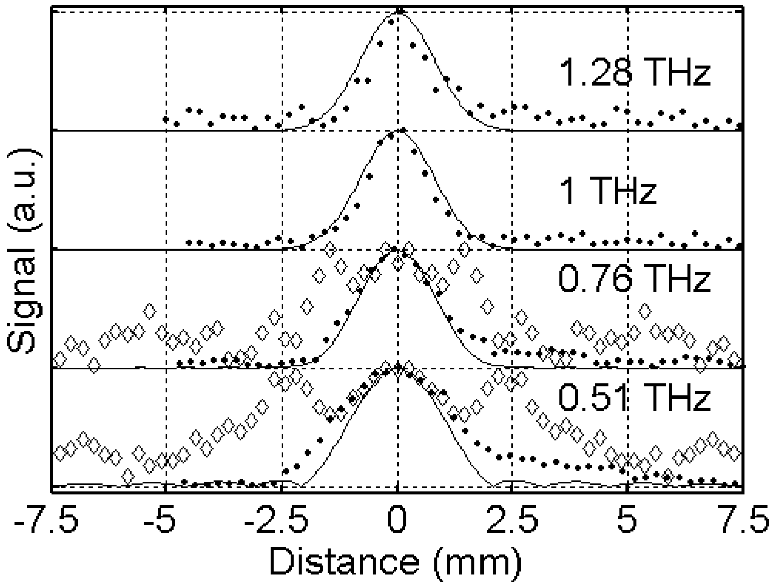

Figure 3.13: Measured beam profiles for the flat (diamonds) and circular (dots) mirrors at the frequencies indicated compared with those predicted by Fourier theory (solid line) for the circular mirror.

We may predict the focal spot size of the beam by first calculating the input beam waist diameters to the test structure. The expected input waist diameters are 17.8, 11.9, 8.9, and 7.1 mm for 0.51, 0.76, 1.0, and 1.28 THz respectively. However, we consider the actual beam presented to the structure to be the product of this (fundamental) Gaussian profile and the 15 mm rectangular aperture function introduced by the finite length of the input silicon cylindrical lens. For simplicity, we assume that the circular mirror functions as a thin lens. It can be shown that such an element produces the complex spatial Fourier transform of an input placed at its front focal plane at the back focal plane of the lens [35]. Therefore, we may calculate the magnitude of the complex spatial Fourier transform of the assumed input field and compare the results to the measurements in the figure. The solid lines in Figure 3.13 are obtained by taking the spatial Fourier transform of the apertured input beam described above. The focal length of the planar optic used in this calculation is fixed at 38 mm for all frequencies, which is the value determined from ray tracing. The discrepancy at lower frequencies may be due to the significant aberrations of a circular surface for a wide, off-axis input beam.

The preceding measurements demonstrate that 2D curved reflective quasioptical elements may be effectively used as focusing elements within the interconnect layer. The incorporation of such elements within the layer introduces no measurable undesirable effects, while serving to concentrate and steer the beam within the guiding structure. No special considerations are made in determining the focusing action of the integrated element, and their behavior is well described by the standard free space techniques used.

Plano-Spherical Lens and Double Slit Elements

In addition to the flat and curved mirrors described in the preceding sections, transmissive and diffractive 2D quasioptical elements have also been demonstrated, although the experimental demonstration was not performed by the author of this dissertation [49]. The full details of the experiment are described in the reference, and a brief description follows:

The parallel plate test structure for these experiments was identical to that used to demonstrate the focusing action of the 2D mirror above. However, due to the use of the transmissive optical elements, the measurement could be made in a simpler fashion. The experimental setup for these measurements is described in Figure 3.14, where the test

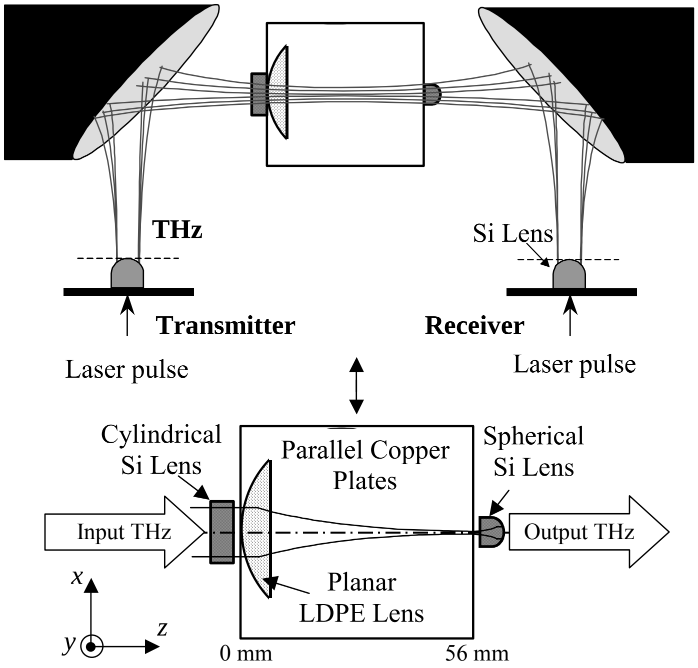

Figure 3.14: THz-TDS arrangement for measuring the focusing action of a 2D LDPE lens. The test structure is 56 mm square (diagram not to scale).

structure is placed at the confocal beam waist of a standard THz-TDS system. In this case the 2D optical element is a 146 μm thick low-density polyethylene (LDPE) lens. The lens is plano-convex, with a radius of 26.4 mm. The lens measures 41 mm in the *x*-direction and 10 mm in the *z*-direction. The focal length of this lens is 51.8 mm, measured from the second (back) principle plane of the lens. This plane lies 3.4 mm to the right of the vertex of the curved lens input, placing the lens focus 0.8 mm inside the test structure output. The test structure output lies at the focus of a silicon spherical lens. The focal region of this lens forms the measurement plane of the system. Due to the long Rayleigh range of the beam at the frequencies of interest, the measurement plane and focal line of the 2D lens are considered to overlap with one another. The results of the predicted and measured results of the focusing action of the LDPE lens are shown in Figure 3.15 below.

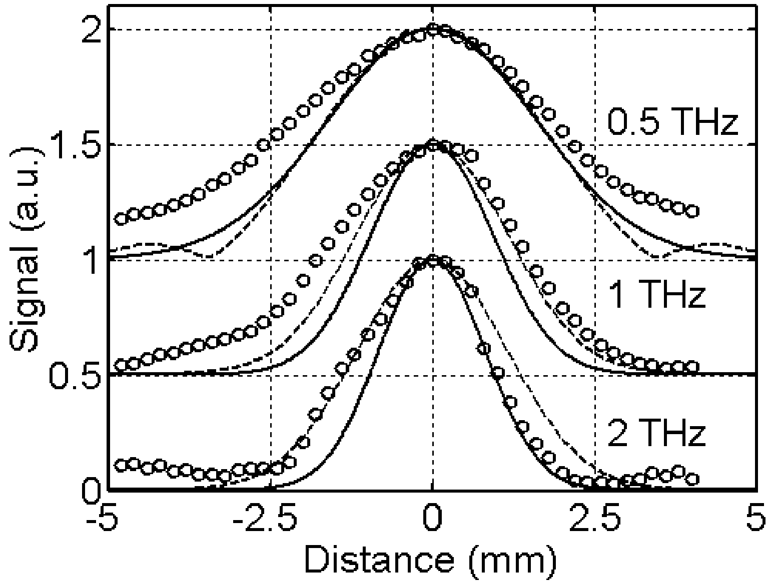

Figure 3.15: Measured beam profiles at the frequencies indicated (open circles) and that predicted by Fourier theory (solid line). The theory used in the published paper is shown as the dashed line.

Here the data (open circles) has been fit using the spatial Fourier transform of the input field patterns (solid lines), which are assumed to be the product of fundamental-mode Gaussians and a 12 mm hard aperture function. The 12 mm hard aperture is a physical aperture in the particular experimental arrangement used. The Fourier transform technique assumes a thin lens with a focal length of 51.8 mm, effectively moving the location of the input field pattern to the back principle plane of the actual thick lens. The method used in the published paper corresponding to this work, which is the result of a polynomial method presented by Urey [51], are plotted as dashed lines for reference. The variation between measured and predicted results is likely due to a combination of effects. However, considering that the measurement is made by translating the 2D lens, the variation is expected to be primarily the result of comatic aberration and uncertainty in the index of refraction of the thin LDPE sheeting [52]. Indeed ray-tracing of the experimental geometry by the first author of [49] indicates that comatic aberration of our experimental arrangement is significant.

The same 2D quasioptical arrangement described above was also used to demonstrate a 2D diffractive structure. Two semi-infinite metal slits were affixed to the stationary input cylindrical lens. The slits were 1 mm wide and spaced by 3 mm, center-to-center. The test structure containing the LDPE lens was incrementally translated in order to measure the diffraction pattern at the device output. The measured data at 1.5 THz along with that predicted by the Fourier transform (solid line) and the simple uniform plane wave illumination calculation of the published article (dashed line) are presented in Figure 3.16 below. Again the variation between theory and experiment are attributed to a combination effects.

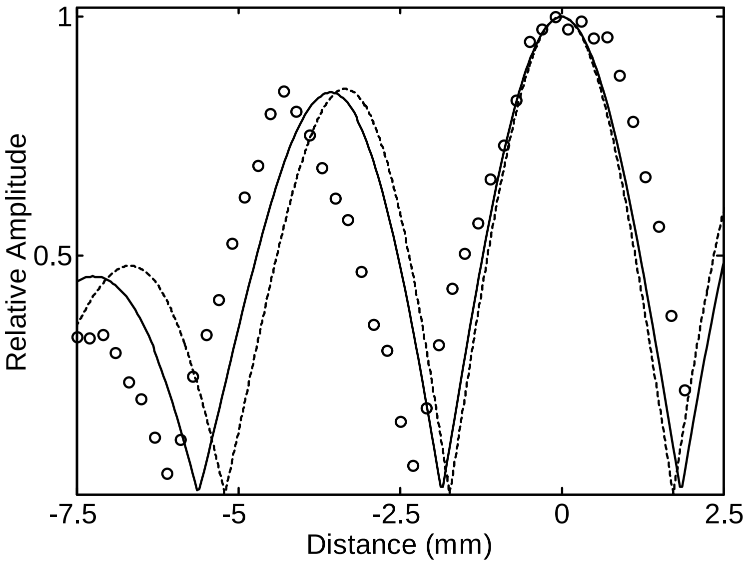

Figure 3.16: Measured 2-slit diffraction pattern at 1.5 THz (open circles) and that predicted by Fourier theory (solid line). The uniform planewave theory used in the published article is depicted as the dashed line.

Thus, 2D reflective, transmissive, and diffractive quasioptical elements have been individually demonstrated to function within the interconnect layer in a manner well described by their 3D equivalents in free space. These demonstrations provide the foundation for more complex TEM-mode guiding structures to be realized should appropriate fabrication techniques be developed. Moreover, if an integrated source and detector are developed for use within the layer, a completely integrated and confocal planar point-to-point system would be possible. Subsequent chapters will describe efforts to develop such a source.

Summary

In the preceding two chapters a new method of coupling THz pulses from a source to detector was experimentally investigated. The planar THz TEM-mode interconnect layer containing 2D integrated quasioptics has shown unprecedented performance for a THz guiding structure. The individual demonstrations are the first of their kind for TEM-mode integrated optical elements at any frequency. This technology guides ultrabroadband THz pulses in the TEM-mode for significant path lengths after multiple quasioptical interactions. The absorption losses of this layer are less than twice the theoretically expected value for a parallel plate waveguide with the same plate spacing. A curved two-dimensional reflective quasioptical element has been shown to spatially compress the electric field within the interconnect layer, working as a thin lens in free space. Incorporated transmissive and diffractive quasioptical elements have likewise been demonstrated to function as their free space 3D counterparts. All of these quasioptical elements maintain the TEM-mode of the guiding structure, working as their 3D counterparts in free space. The demonstrated interconnect layer and the incorporated 2D quasioptical elements push the envelope of guiding structure technology to allow for low-loss TEM-mode propagation of sub-ps pulses for significant lengths after multiple quasioptical interactions. The devices demonstrated above can be considered as components of a 2D optical table and may be analyzed with standard optical treatments. Now that several passive components of this high-performance guiding structure have been demonstrated, the emphasis of this document will be shifted to the incorporation of active devices within the same structure.

Chapter 4

Parallel Plate THz Source Demonstration and Characterization

This chapter describes a new class of ultrafast THz source, called the parallel plate Terahertz transmitter, or PPT transmitter/source. As the name implies, this source consists of two parallel metal plates separated by a semiconductor. A representative device is depicted in Figure 4.1. The PPT transmitter was conceived in an attempt to integrate an ultrafast THz source within the 2D TEM-mode interconnect layer described in previous chapters. This source represents the next step in guided wave point-to-point communication at THz frequencies within the 2D TEM-mode interconnect structures described in previous chapters. This device is intended to be a powerful source of direct optoelectronic excitation of TEM-mode guided waves. This chapter describes the first experimental demonstration and characterization of the PPT transmitter.

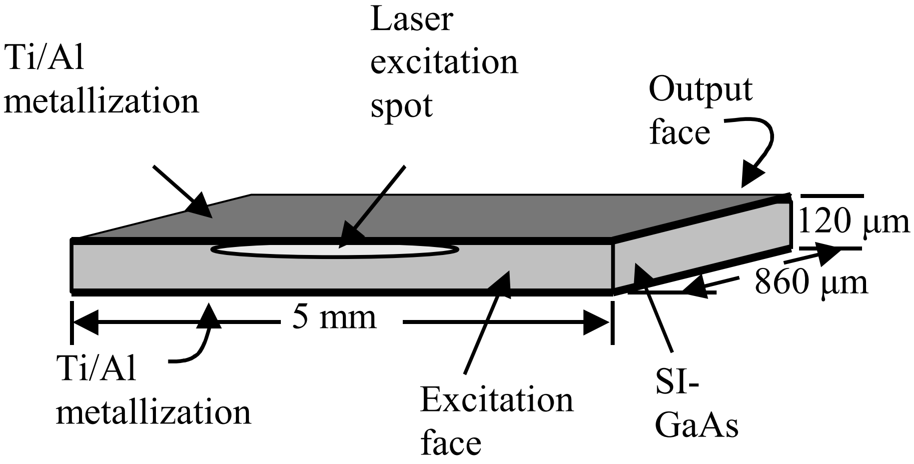

Figure 4.1: Example PPT source made from semi-insulating Gallium Arsenide.

At first glance this chapter might appear as a bit of a digression from the topic of two-dimensional TEM-mode quasioptics. However, the experiments described herein are the first attempt at generating TEM-mode THz radiation for the express purpose of point-to-point all guided wave communication at these frequencies. While one other guided wave THz transmitter has been recently demonstrated, it has not yet been characterized [53,54]. The source described in subsequent pages is characterized using the standard THz-TDS arrangement. Ideally the source would be demonstrated entirely within the new guiding structure. However, a detector of guided wave radiation has not yet been demonstrated or characterized. We therefore demonstrate the new transmitter in the otherwise well-known THz-TDS system. The direct detection of the TEM-mode of the guiding layer is demonstrated at the end of this chapter. This chapter is approached as a collection of experimental observations attempting to carve out the parameter space of the overarching theories. Comparisons are made to available theory and to standard devices whenever possible. Portions of the data contained in this chapter have been previously published [55].

Die Manufacture

We first turn our attention to the fabrication of PPT transmitters. The general procedure is as follows:

A 500μm thick semi-insulating <100> oriented GaAs (SI-GaAs) wafer is diced into several large pieces, the typical geometry of these pieces is 10 mm x 20 mm x 500 μm. The wafer piece is then mounted to an aluminum backplate using 7036 blanchard wax, a common semiconductor mounting wax. Several glass shims are also bonded to the backing plate around the wafer piece using blanchard wax. These shims are of a uniform thickness, and allow the wafer piece to be thinned to a uniform thickness as well. The wafer piece is thinned by hand using progressively finer grits of automotive sandpaper and water or soapy water as a lubricant. The sandpaper is attached to a laboratory grade granite tool flat. After thinning the GaAs piece to the appropriate thickness, the wafer piece is polished using jeweler's rouge and water. The process leaves a highly polished finish, with minimal rounding of the wafer piece edges. Throughout this work, all experimentally investigated devices have been thinned by hand-polishing a single side. The hand polished side is used as the device cathode and the device anode side has an as received high-polish. The entire polishing and thinning process may potentially be bypassed if a thin polished wafer is purchased.

After thinning, the wafer piece is removed from the backing plate using room temperature acetone. After removal, the wafer piece may cleaned in a cleanroom via a standard GaAs cleaning process, or the same cleaning process may be used outside of a cleanroom. Device performance does not appear to be adversely affected by processing outside of a cleanroom. For the specific GaAs cleaning process used, the wafer piece is placed in a series of baths beginning with 65°C (boiling) Ensolv for 5 minutes per side. The wafer piece is then transferred to room temperature acetone for 5 minutes per side, and then to room temperature methanol for 5 minutes per side. Any oxide present on the surface is then removed in a room temperature 1:40 volume ratio of 12M hydrochloric acid to water solution for 2 minutes per side. The wafer piece is then dried with dry nitrogen. Within 30 minutes of the deoxidation process, the wafer is plasma etched for 30-45 minutes per side in 200 mtorr of forming gas (5% H/95% Ar) with 200 W of RF power. After plasma etching, the device is metallized in a thermal evaporator with nominally 100 nm of titanium and 400 nm of aluminum on both sides. After metallization, the wafer piece is bonded to a silicon substrate using blanchard wax, and diced to size using a semiconductor dicing saw.

After dicing, the individual dice (chips) are separated from the substrate and cleaned in room temperature acetone. Typical die geometries are 5 mm x 900 μm x 120 μm. While the diced edges of the PPT transmitter are generally not as smooth as cleaved facets along crystallographic planes, atomic force microscopy of the diced edges shows that surface peak to peak roughness is less than 200 nm. Therefore, the diced edge structure is not expected to significantly affect the propagating THz frequencies. However, throughout this work deleterious effects were observed when the device edges became excessively chipped or jagged.

Successful PPT source fabrication requires excellent metal adhesion to the semiconductor. To date metallization has been applied via thermal evaporation and electron beam evaporation. Substantially improved results were obtained through the use of the E-beam evaporator, although only a single experiment has been conducted [56]. Often, the applied metallization begins to fail due to poor adhesion during dicing. As the dicing saw cuts the unpatterned metal and semiconductor, it often begins to lift the metal from the semiconductor near the saw kerf. This process may occur locally, with the metal delaminating from a region within approximately 50 µm from the kerf, or, upon subsequent dicing, a majority of the applied metal may lift from many or all devices. The extent of the effect appears to be dependent on surface preparation of the wafer, conditions within the evaporator, and dicing techniques. Long duration plasma etching in forming gas appears to increase the metal adhesion slightly.

The present failure rate for PPT sources with Ti/Al metallization is over 90 percent. However, with more emphasis placed on forming highly adherent metal coatings, this rate is expected to lessen substantially. Dicing (and cleaving) methods may be examined in order to minimize their effects on metal delamination. Metal adhesion might also be improved if the electrodes are annealed after evaporation but before dicing. Putting fabrication issues aside, we may consider the individual PPT dice to exist in the desired form and one may now assemble a PPT transmitter.

Transmitter Construction

To assemble a PPT transmitter, individual PPT dice are packaged in a parallel plate aluminum structure serving as a heatsink, mechanical support, and providing electrical contact to the device electrodes. This structure also provides a means to attach a high resistivity silicon collimating lens to the output face of the die. A schematic representation of this mounting structure, referred to as the PPT transmitter core, is shown in Figure 4.2.

The subsequently attached silicon lens is large and fabricated from relatively conductive high-resistivity Si material. Therefore, installing the lens places a relatively low resistance in parallel with the very high PPT die resistance. It was determined early in device development that the silicon lens must therefore be electrically isolated from the bias electrodes. For a majority of this work, isolation was achieved by placing a 2.5 μm thick layer of Mylar between the lens and electrode structure. However, recent experiments have been performed with electrical isolation achieved by thermally growing a ~1 μm thick layer of silicon dioxide on the lens surface. There is no observable effect on performance for either method of isolation. The PPT core assembly is installed in an assembly of commercially available optomechanical hardware. The assembled transmitter is a complete unit containing a focusing lens for the laser excitation, a means to independently translate the die/electrode structure and silicon lens, and a kinematic baseplate such that the transmitter may be reliably and repeatedly placed in a THz-TDS system. With the transmitter assembled, the PPT transmitter can be characterized in a standard THz-TDS arrangement.

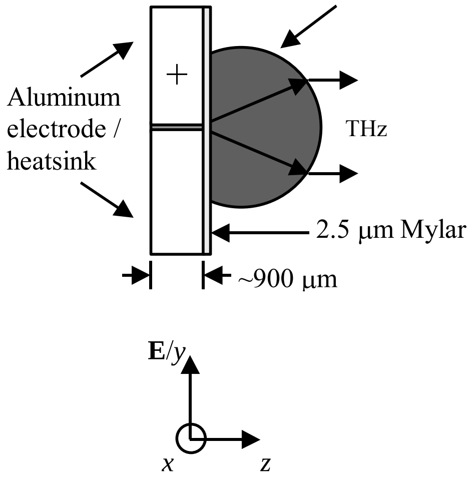

Figure 4.2: PPT transmitter core illustrating the mounting structure and electrical isolation of the silicon lens.

Experimental Demonstration

The PPT transmitter has been investigated in a variety of experimental arrangements. This section describes some of the experiments undertaken and their results. The PPT transmitter is shown to be capable of generating large THz signals, with varying spectra under a variety of experimental conditions. Wherever possible the data is compared to that from standard transmitters. Although the complex behavior of the PPT transmitter is not fully understood, the experimental data offers clues to the true nature of its operation.

THz Generation via Photoconductive Switching

An original intent of implementing the PPT transmitter in a free space coupled configuration was to increase the efficiency and/or the output power of the PPT relative to the "F-chip" transmitter. The PPT was only considered for photoconductively switched operation. This section examines the behavior of a biased PPT transmitter in a standard THz-TDS arrangement, and compares it to that of the standard F-chip.

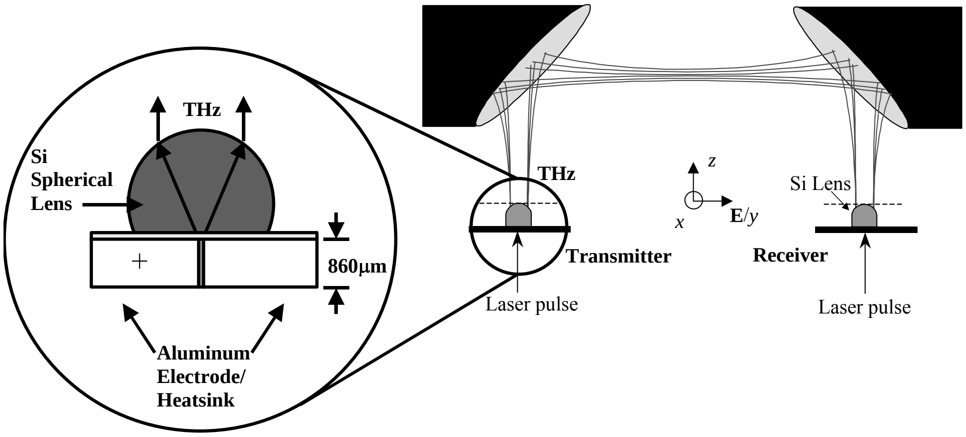

Figure 4.3: THz-TDS arrangement for comparing the PPT and F-chip transmitters.

The transmitter was placed in a standard THz-TDS arrangement with a standard LT-GaAs receiver. Figure 4.3 depicts the TDS system with the PPT transmitter installed. The coplanar metallization of the receiver consisted of two 10 µm wide lines spaced by 30 µm, it is henceforth referred to as an LT-GaAs 10-30-10 receiver. All receivers used in this work, regardless of transmission line spacing, have a symmetric dipole structure with a 5 µm gap placed between the lines. The PPT transmitter was biased at 70 V and excited with 150 mW of average laser power. The laser excitation spot formed an oval with a major axis parallel to the PPT electrodes. The size of this spot was 230 µm by 15 µm, and the spot was placed near the device anode. In order for the F-chip transmitter to be operated at acceptable current consumption levels, the excitation spot was reduced to a 10 µm diameter circular spot. This reduced spot limited the maximum laser excitation power to around 15 mW. In this configuration the PPT transmitter was compared to an F-chip transmitter.

Figure 4.4 compares the time-domain signals and spectra of the resultant THz pulses. In this instance we can see that the peak THz signal amplitudes are roughly the same for the two devices, at approximately 10.5 nA. However, using receivers optimal to each transmitter, the maximum signals recorded in our labs for each type of transmitter operating in photoconductively switched mode are 50 nA for the PPT transmitter and 20 nA for the F-chip. In obtaining the maximum signals a LT-GaAs 10-50-10 receiver was used for the PPT transmitter, while a LT-GaAs 10-30-10 receiver was used for the F-chip. The PPT transmitter is therefore shown to be a powerful source of freely propagating THz radiation, and is comparable to standard, well-developed sources.

The PPT source is itself a short length of dielectric filled parallel plate waveguide. As such, excitation of this device may be approximated by matching an excitation field of finite extent, representing the laser spot (and generated photocurrent), to the guided modes of the source die. This may be accomplished mathematically using the overlap integral as in [57, p. 172]. The revealing point of this treatment is that for excitation near the anode, all of the modes in the spectrum shown in the lower panel of Figure 4.4 are excited. The dashed vertical lines in the figure indicate the first eight mode cutoff frequencies in the source die. Some of the structure in the spectrum coincides with these frequencies. However, due to the lack of beating phenomena in the spectrum, higher-order mode excitation in the source die appears as a loss process to the detected TEM-mode.

Were the PPT integrated with our 2D quasioptical structures, which are air-filled, higher-order modes in the die would not cause detectable higher-order mode excitation in the bulk air-filled guide. In our standard 100 μm thick guides the TM_1 mode lies within our spectrum, however, it is undetectable due to anti-symmetry. Therefore, even with several excited modes in the PPT transmitter, we may consider only the TEM mode in the context of our 2D optical table.

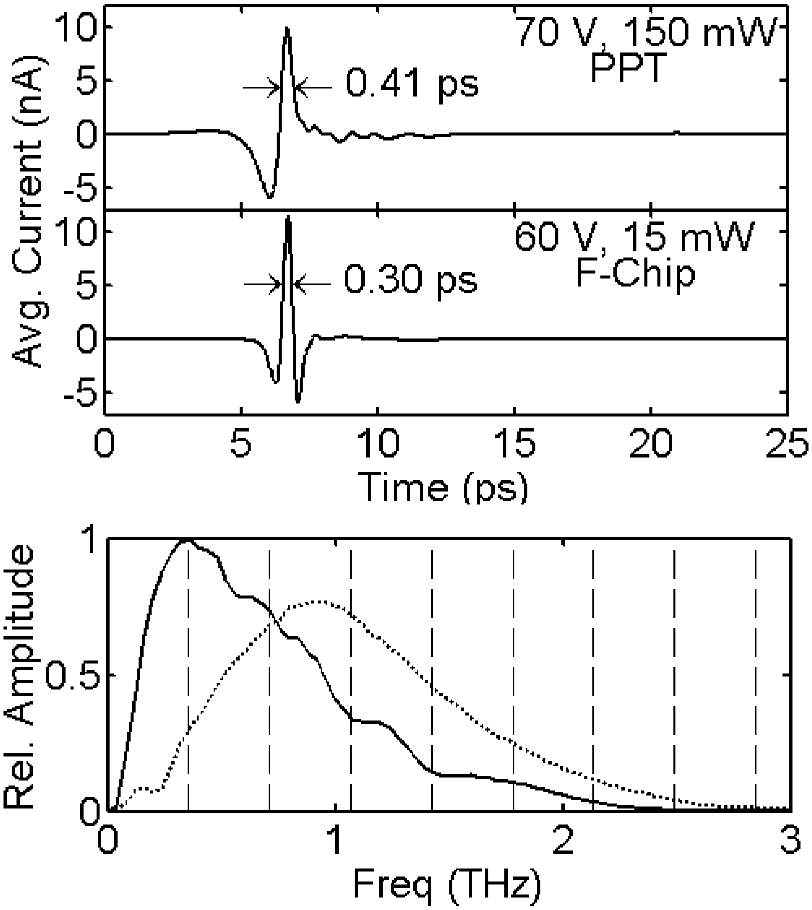

Figure 4.4: Measured THz pulses and corresponding spectra for the PPT (solid) and F-chip (dashed) sources under the conditions identified in the figure. The first 8 higher order mode cutoff frequencies are depicted as dashed vertical lines.

Despite comparable peak signal amplitudes in the experiment above, the two transmitters exhibit significantly different output spectra, as shown in the lower panel of Figure 4.4. This is tentatively attributed to two separate phenomena: the aforementioned higher-order mode excitation in the transmitter itself and non-optimal optical coupling of the PPT transmitter to the receiver. It should again be noted that the excitation power for the PPT transmitter is 10 times that for the F-chip. This implies that the PPT transmitter is in fact less efficient than the F-chip, despite a predicted increase due to bias field improvement.

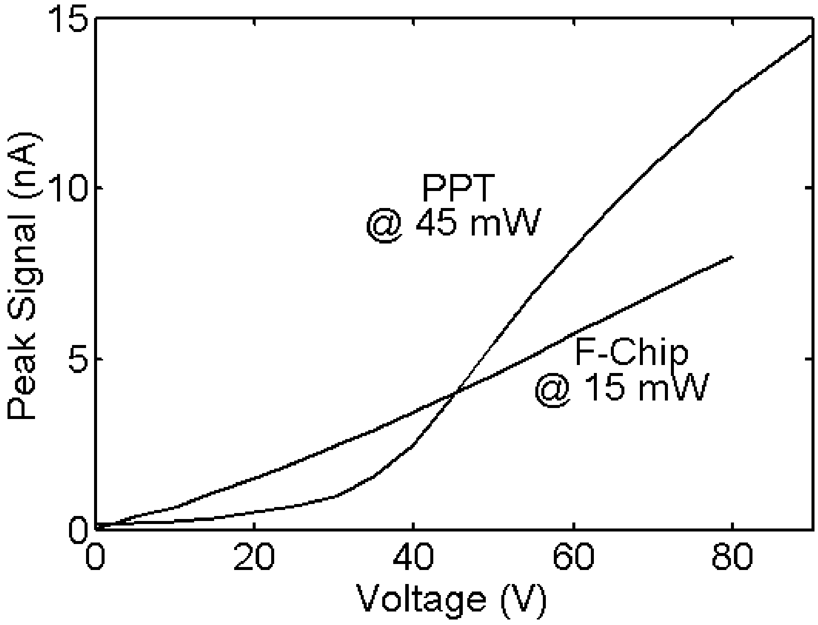

Figure 4.5: Peak measured THz signal vs. bias voltage for the PPT and F-chip transmitters as the excitation powers indicated.

Signal vs. Applied Bias

In this experiment the THz signal amplitude and transmitter bias current were recorded as a function of bias voltage for both the F-chip and PPT transmitters. We may say that the radiated THz power for a photoconductively switched transmitter is proportional to the charge acceleration [58]. In the simplest approximation of ballistic carrier acceleration, the acceleration is proportional to the bias electric field. Thus, the radiated THz power should be a linear function of bias voltage. Figure 4.5 shows the peak THz signal amplitude versus bias voltage for the PPT and F-chip transmitters at a constant excitation power. The F-chip varies as expected, that is the peak THz signal is a linear function of the applied bias voltage. However, the PPT transmitter is not so well behaved.

As illustrated in Figure 4.5, the generated signal versus bias voltage characteristics of the F-chip transmitter are linear. This is expected where only the acceleration of the carriers is affected by increasing voltage. However, the PPT transmitter is markedly nonlinear, hinting at the possibility of other parameters being affected by bias voltage. While the origins of the nonlinearity are not well understood, at least two possibilities exist. The nonlinearity of the curve may be due to a voltage dependent coupling to the spectrum of guided modes within the PPT transmitter, and the decreased sensitivity of the receiver to such modes. Voltage dependent mode coupling might be due to a spatially varying bias field that is voltage dependent for the PPT transmitter, which is likely due to space charge effects.

This curve might also reveal more subtle factors affecting the PPT source. That is, the PPT transmitter appears to exhibit a threshold type behavior, occurring in this instance at around 40 V. This behavior is similar to that observed by Ralph for the larger coplanar devices he studied [59]. This threshold behavior was attributed to double injection processes at the anode. However, it should be noted that in Ralph's experiment annealed Au/Ni/Ge ohmic contacts were used. If double injection processes in the PPT transmitter are responsible for the non-linearity of the THz vs. bias curve, one would expect the concentrated bias field of the F-chip to produce similar behavior, but at lower bias voltages, as the necessary fields for double injection at the anode to occur would be present at lower voltages.

Signal vs. Excitation Power

Neglecting saturation effects, the number of photocarriers generated per laser pulse is proportional to the incident laser pulse energy. We therefore expect a linear increase in photocurrent, and hence generated THz, with increasing optical power. However, if we incorporate absorption saturation at the excitation wavelength the generated signal versus power curve should become nonlinear. For a two level system neglecting pulse repetition rates and carrier lifetime in the short pulse limit, the number of carriers generated for a single pulse is [60],

$$N_p = N_1\left(1-\exp(-\Gamma_t/\Gamma_s)\right) \tag{4-1}$$

where N_1 is the available number of carriers within the excitation volume in the valence band, Γ_t is the total energy in the excitation pulse divided by the excitation area, or excitation pulse fluence, and Γ_s is the material saturation fluence. Γ_s is a material constant related to the absorption cross-section,

$$\Gamma_s = \frac{hf}{2\sigma_a} \tag{4-2}$$

where h is Planck's constant (6.626×10^{-36} J·s), f is excitation frequency, and σ_a is the absorption cross-section at the excitation wavelength. The saturation fluence for the interband transition of GaAs is typically less than 50 μJ/cm^2 [61]. Under the excitation conditions used in the experiment for each transmitter, the saturation fluences correspond to an average laser power of 3.5 mW for the F-chip transmitter and 130 mW for the PPT transmitter.

The excitation of our transmitters is achieved using a 90 MHz repetition rate Ti:sapphire laser. The laser pulses therefore occur at 11.1 ns increments. This pulse spacing is on the same order as the published approximate carrier lifetime of 10 ns in GaAs [63]. As such, instead of the convenience of (4-1) we must monitor the relative populations of the valence and conduction bands to determine an appropriate value for N_t. The population of each level is described by the pair of differential equations:

$$\begin{aligned} \frac{dN_1}{dt} &= \frac{-N_p}{\tau_{rep}} + \frac{N_2}{\tau_{recomb}} \\ \frac{dN_2}{dt} &= \frac{N_p}{\tau_{rep}} - \frac{N_2}{\tau_{recomb}} \end{aligned} \tag{4-3}$$

where N_1 and N_2 are the populations of the ground and excited state, τ_{rep} is the reciprocal of the laser repition rate, τ_{recomb} is the carrier lifetime, and N_p is described by equation (4-1).

Figure 4.6 and 4.7 show the THz signal vs. excitation power for the PPT and F-chip transmitter at a fixed bias voltage on log-linear and again on linear-linear scales. From these curves it is again apparent that, at least under the operating conditions and optical coupling used in these experiments, the PPT transmitter is significantly less efficient than the F-chip. The PPT transmitter is saturating in the form of equation (4-1). The same theory should be used to fit the behavior illustrated by the F-chip device. However, the curve cannot be fit without floating a parameter. It should be noted that the F-chip is operating at a much more saturated level than the PPT device. This fact may explain why the simple model of absorption saturation does not work for the F-chip. At highly saturated levels, it may be more appropriate to consider bias field-screening effects as a function of excitation power [62]. For the solid line shown in the figure, which is a plot of equation (4-1), the laser excitation spot diameter was taken as 230 μm x 8 μm and Γ_s was taken as 50 μj/cm^2, the only floating parameter is a constant scaling factor relating transmitter current to received signal current. The dashed line in these figures is a plot of the expected signal saturation, by equations (4-3) when carrier lifetime and pulse repetition rate are considered. This curve approaches that predicted by equation (4-1) for decreasing carrier lifetimes, indicating that our experimental carrier lifetime could be significantly shorter than the expected value. A possible explanation for a decreased carrier lifetime lies in the excitation edge structure. The edges of the PPT device are cut from the parent wafer using a dicing saw. The cut surface is neither a crystallographic plane nor a highly polished surface. Therefore, we expect a high number of defects at the device edges, which could serve to lower the carrier lifetime. Clearly, additional experimental work is required to fully understand the observed signal saturation behavior.

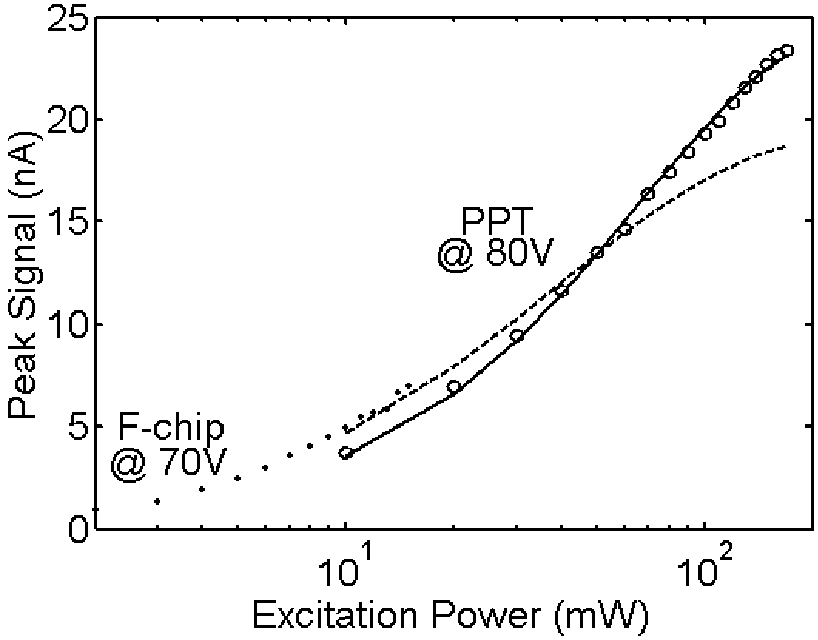

Figure 4.6: Peak measured THz signal vs. excitation power for the PPT (open) and F-chip transmitters (solid). The solid line depicts the predicted behavior when saturation of the interband transition is incorporated neglecting carrier lifetime under pulsed excitation. The dashed line accounts for a 10 ns carrier lifetime (linear-log scale).

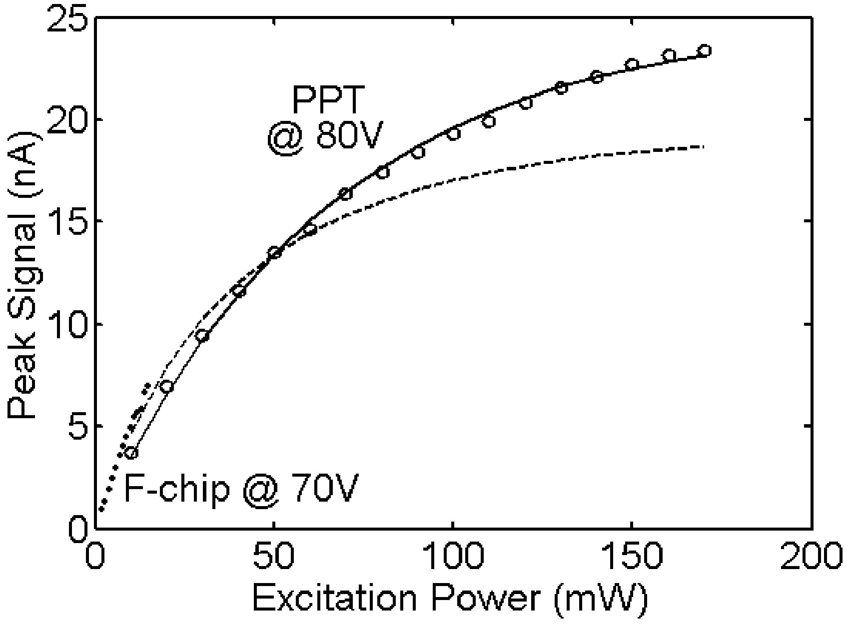

Figure 4.7: Peak measured THz signal vs. excitation power for the PPT (open) and F-chip transmitters (solid). The solid line depicts the predicted behavior when saturation of the interband transition is incorporated neglecting carrier lifetime under pulsed excitation. The dashed line accounts for a 10 ns carrier lifetime (linear-linear scale)

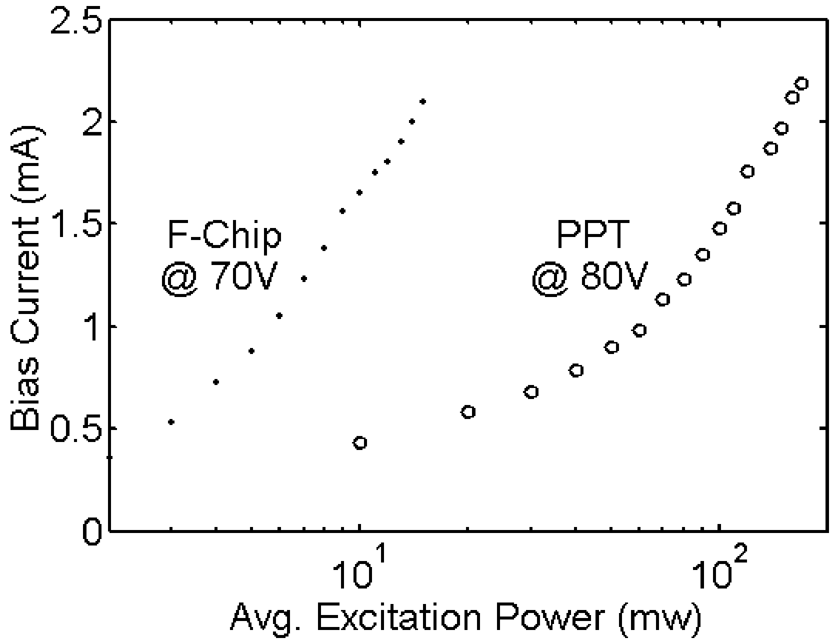

Figure 4.8: Source bias current vs. excitation power for the F-chip and PPT transmitters at the bias voltages indicated. (linear-log scale)

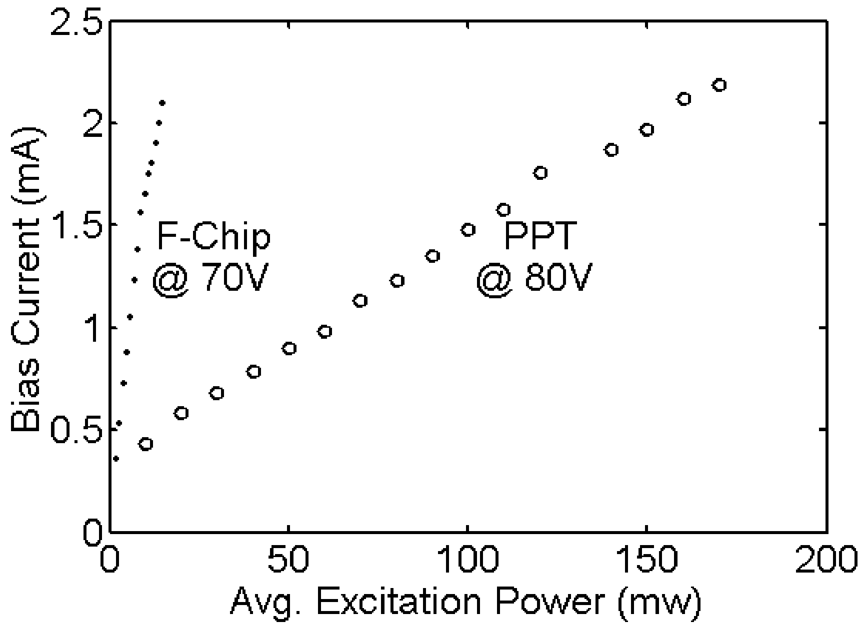

Figure 4.9: Source bias current vs. excitation power for the F-chip and PPT transmitters at the bias voltages indicated. (linear-linear scale)

Figure 4.8 and 4.9 plot the bias currents measured at the two sources during the experiment depicted in Figure 4.6 and 4.7. Interestingly, while the PPT transmitter is not as efficient as the F-chip in converting laser power to THz signal, it is much more efficient in terms of bias current. Moreover, for both the PPT and F-chip transmitters, there is a nonlinear relationship between bias current and measured THz signal. In particular we note that for the PPT transmitter the detected THz signal is saturating as a function of transmitter laser excitation power. However, the PPT transmitter bias current appears to be a linear function of excitation power.

Operation via Optical Rectification

While the PPT transmitter was developed to be a photoconductively switched source, significant signal amplitudes were observed from the device in the absence of a bias field. Originally these signals were thought to originate from the acceleration of carriers in the Schottky depletion region(s) of the device. This field is oriented in opposite directions as in the case of the surface field, normal to each device electrode. Signal generation may also be possible from a possible surface field related to the excitation surface. However, several observations have discredited these possibilities.

The first observation simply acknowledges that optical rectification is not only possible, but is expected for the PPT transmitter. For the PPT transmitter, recall that the illuminated face of the GaAs has been diced from a <100> oriented wafer. The dicing process therefore reveals a surface normal to the (100) plane. In general, this surface is of a non-centrosymmetric electro-optic material and should therefore be expected to produce a THz signal via optical rectification. In fact, if the wafer is diced (preferably cleaved) along the proper axis one may reveal the (110) plane, which has been previously exploited for THz generation via optical rectification [64].

The second observation directly discredits the possibility of THz generation due to the surface field (or Schottky depletion region) in the absence of a bias. Recall that the surface or Schottky fields are oriented normal to the planes of the wafer surfaces. As such, we expect two surfaces to contribute to the detected THz signal generated from such fields. One component should be maximized near the anode metallization and the second component should be maximized near the cathode metallization, in each instance the field is polarized out of the surface. We therefore expect the bias field (and hence the radiated THz) to be anti-symmetric, or dual lobed when examined as a function of position between electrode surfaces. As will be shown in Figure 4.12, the generated signal amplitude versus excitation position between the device electrodes is neither anti-symmetric nor dual lobed as would be expected from identical but oppositely polarized depletion fields. While the diced edge normal to the device electrodes could theoretically also exhibit a surface field, radiation generated from this field would tend to produce a standing wave between the transmitter plates. FDTD modeling of this type of excitation predicts that the primary excited mode of the relevant polarization for the transmitter will be the antisymmetric (and hence essentially undetectable) TM_1-mode of the parallel plate die. Lastly, if the excitation face were a true (110) crystallographic plane, it would exhibit no surface field [65] from which to generate THz.

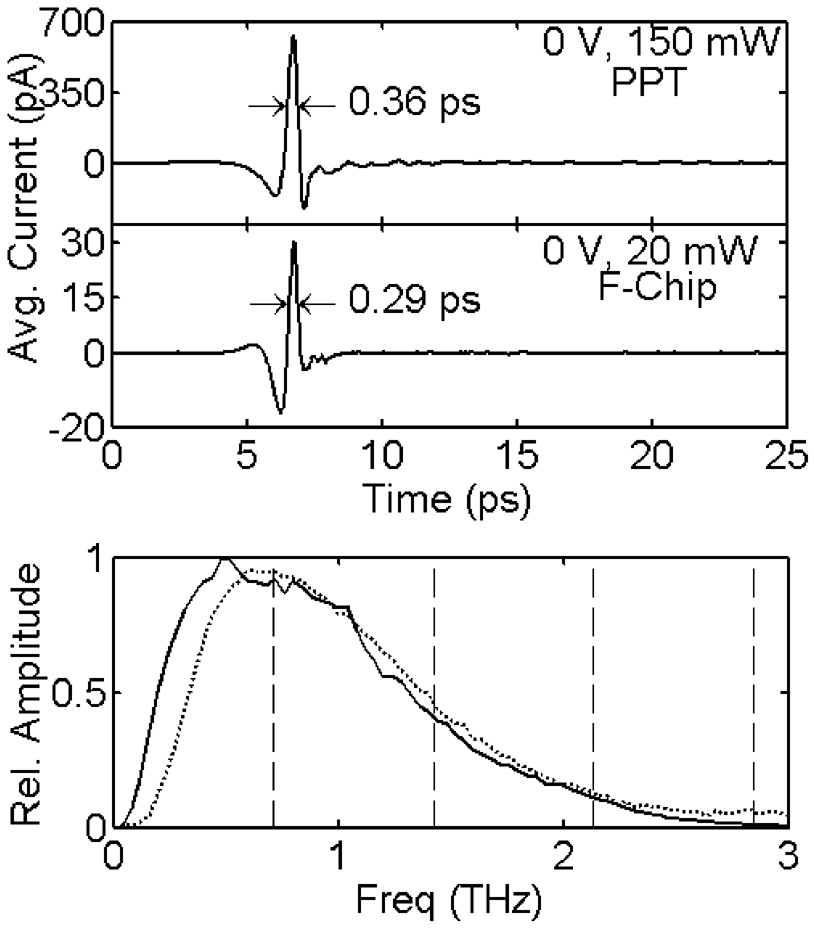

Figure 4.10 Measured THz pulses and corresponding spectra for the PPT (solid) and F-chip (dashed) transmitters under the conditions listed in the figure.

To experimentally investigate the origin of the signals obtained with no bias voltage applied, the F-chip and PPT transmitters were investigated as in the photoconductively switched experiment described previously, except no bias voltage was used. Figure 4.10 shows time and frequency-domain data for the F-chip and PPT transmitters. The time-domain data for the F-chip is taken from the average of 9 scans. The frequency domain data for the F-chip is multiplied by a factor of 20 to facilitate comparison. The PPT data is unscaled data from a single scan. We can see that the spectrum produced by the PPT transmitter is smoother and broader than for the biased case of the same transmitter shown in Figure 4.4. The increased signal bandwidth, relative to the biased PPT transmitter, is consistent with the increase in bandwidth expected for optical rectifying transmitters relative to those relying on carrier acceleration. Therefore, all experimentally and theoretically observed phenomena require that the device generate THz via optical rectification in the absence of an applied bias field. In comparing the PPT transmitter under no bias to the F-chip transmitter with no bias, we observe that the FWHM bandwidth of the PPT is appreciably wider than that for the F-chip in this experiment. The difference in spectra between the F-chip and PPT is most pronounced at lower frequencies. In the above figure, only the first four *even* mode cutoff frequencies of the PPT transmitter are shown as dashed vertical lines. Symmetry requires that the odd modes of the transmitter not be excited for excitation centered between the plates, which will be explained in the next section.

Signal as a function of position

Whether the PPT transmitter was operated with an applied bias voltage, or not, the laser excitation spot was moved in order to maximize the detected THz signal. However, the spot location corresponding to a maximum detected signal for each case was not the same for both methods of operation. Therefore, the THz signal magnitude versus excitation spot position was mapped in a series of experiments with and without an applied bias voltage as depicted schematically in Figure 4.11. A circular excitation spot was used to maximize spatial resolution. The results of these experiments are depicted in Figure 4.12.

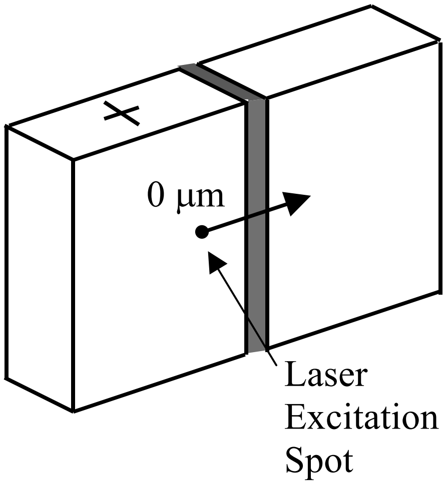

Figure 4.11: Schematic depiction of the experiment used to determine the peak measured THz field as a function of generation spot position.

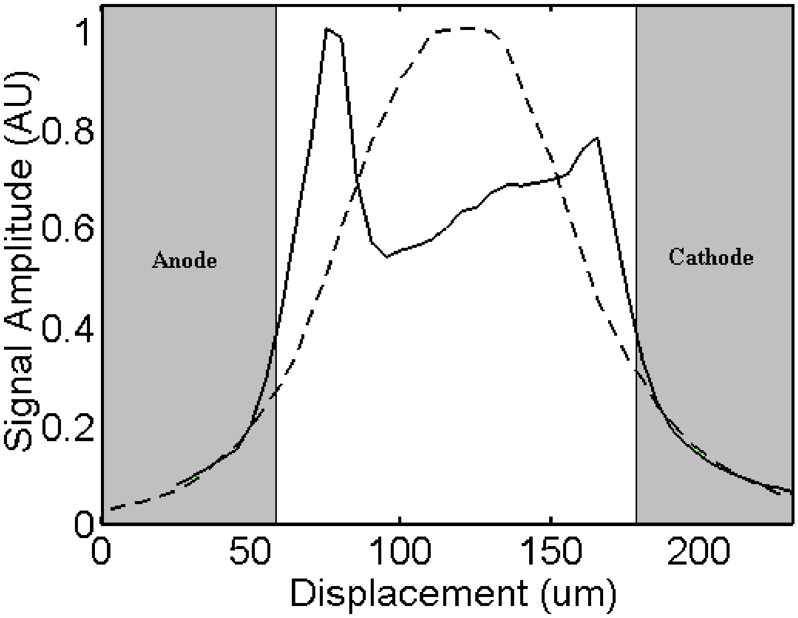

Figure 4.12: Individually normalized THz amplitude versus displacement along an axis normal to the device electrodes for a 120 μm thick PPT transmitter with a 70 V applied bias (solid) and with no bias (dashed).

Figure 4.12 plots the detected THz field amplitude versus displacement along an axis normal to the electrodes, where each curve has been normalized to its own maximum value. These two curves correspond to a 120 μm thick PPT transmitter with a 70 V applied bias and with no applied bias. The spatial resolution of this experiment is limited by the excitation laser spot size and rough surface structure of the excitation face. From the figure we can see that the THz generated when the device is biased is maximized near the anode. As THz amplitude is directly proportional to the bias field magnitude, this curve reveals a highly non-uniform bias field present in the PPT transmitter when operated under an applied bias voltage. The non-uniformity of this field, showing pronounced enhancement at the anode has been previously described for coplanar devices [59]. However, when the PPT transmitter is operated without an applied bias, the detected THz amplitude shows a smooth dependence on position. The peak of this curve is located midway between the device electrodes. In this position any aperturing effects are at a minimum, and THz production via optical rectification is maximized. We note that this curve is neither dual-lobed nor antisymmetric, indicating that generation is not due to surface or Schottky depletion field effects.

The generation of significant signal amplitudes via optical rectification came as a pleasant surprise in the development of the PPT transmitter. In particular, the ability to generate substantial signals in the absence of a bias field offers great potential for the monolithic integration of planar quasioptical elements and sources (and detectors). The development of monolithic TEM-mode integrated quasioptical systems may be made significantly easier by removing the need for a high-voltage supply and the necessary bias electrical contacts and using the PPT source in optical rectification mode.

Furthermore, this mode of operation exhibits a smoother spectrum with higher FWHM bandwidth than that for the biased case, which is evidenced by the faster temporal waveforms generated. The PPT transmitter is a unique THz source in that it demonstrates useful and unique signal characteristics via two completely different methods of generation. Its ability to be readily incorporated within our 2D TEM-mode quasioptical systems insures its future application.

Direct Excitation of a Parallel Plate Guide

While the PPT transmitter is itself a small length of dielectric filled parallel plate guide, the source was used to excite a small air filled parallel plate guide. The experiment described in this section was a driving force for the development of the integrated quasioptical elements described in Chapters 2 and 3. In this experiment, the standard THz-TDS system was replaced with a PPT source placed directly within a 25 mm long air filled parallel plate structure. The aluminum plates of the structure were biased directly. The output of the structure was measured using the previously described fiber coupled beam profiling system of Reiten et al [50]. Figure 4.13 illustrates the waveguide structure with a THz pulse several millimeters from the waveguide output. The upper panel of the figure is to scale. This figure illustrates the unconstrained spreading of the beam generated from the PPT transmitter in a standard parallel plate guide. The observation of this spreading along the unguided axis helped lead to the development of the planar quasioptical elements in Chapter 3. This experiment also demonstrated for the first time photoconductively switched excitation of a parallel plate structure.

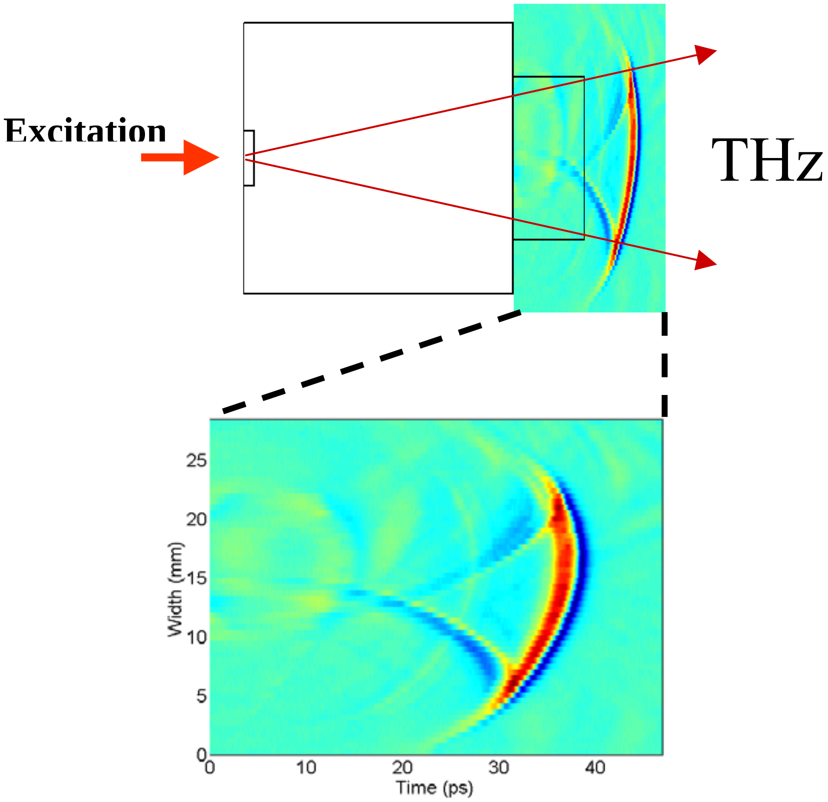

Figure 4.13: Beam profile of a directly excited parallel plate waveguide along an axis parallel to the guide plates. The upper panel is to scale and indicates the measurement window. The lower panel is a close-up of the measurement window.

After performing the measurements above using the fiber coupled scanning receiver, a 10-50-10 SOS receiver was situated directly at the device output. In order to prevent shorting the receiver electrodes, the sapphire side of the SOS wafer was contacted to the parallel plate structure. Thus, in this configuration the direct excitation of the waveguide structure by the PPT transmitter was directly optoelectronically detected with a conventional receiver. No quasioptical elements were incorporated within the parallel plate structure. The detected THz pulse is shown in Figure 4.14. The origin of the low-frequency ringing in the scan is unknown, while the sharp negative spike occurring approximately 10 ps after the main pulse is due to reflection within the transmitter die. The spectrum of the pulse of Figure 4.14 is shown in Figure 4.15. The relatively long-duration pulse width is reflected by its sub-THz spectrum. However, the actual spectrum of the pulse, were the reflections removed, is likely smoother than that indicated by the figure. Though the results are preliminary, this experiment demonstrates the direct excitation and detection of a picosecond TEM-mode pulse of THz radiation in a TEM-mode guiding structure. It should be noted that for an air-filled parallel plate structure of 117 μm spacing as used in the experiment, the cutoff frequency of the TM_1-mode is ~1.3 THz. Thus, the measured signal in Figure 4.14 is contained entirely in the TEM-mode.

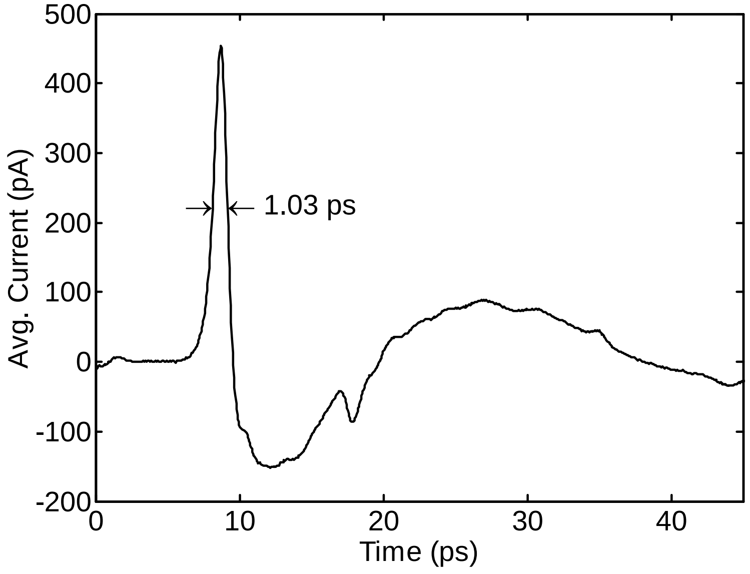

Figure 4.14: Directly measured THz pulse for directly excited parallel plate waveguide. The FWHM pulsewidth of the main peak is indicated by arrows.

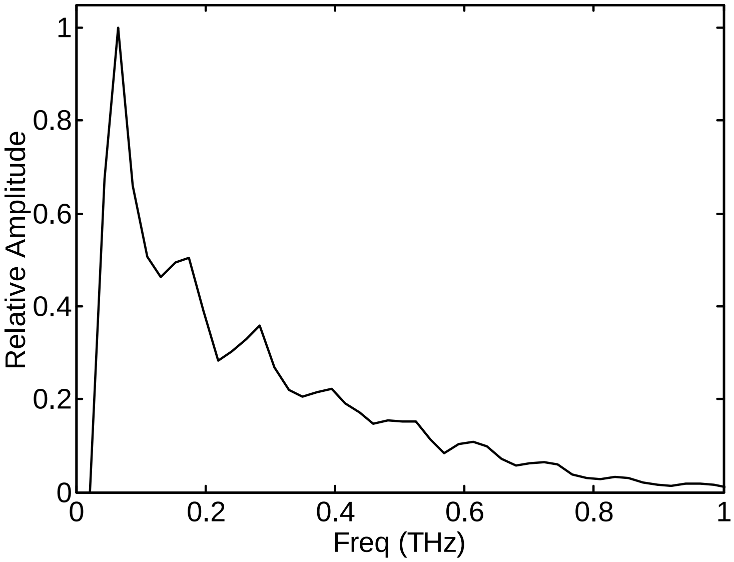

Figure 4.15: Amplitude spectrum corresponding to the pulse in the figure above.

Summary

In the preceding chapter a new type of photoconductively switched transmitter has been demonstrated. Experimentally, the PPT transmitter is shown to be a powerful source of THz radiation capable of high-bandwidth operation. Although simultaneous operation at high-power and high-bandwidth has not yet been achieved, the device easily generates sub-ps pulses of THz radiation in both modes of operation. The device is also shown to have several features and drawbacks relative to standard PC switched THz transmitters. The features include ease of fabrication, mechanical robustness, and increased power handling capacity. Most importantly the PPT source is capable of direct excitation of the TEM-mode in planar guiding structures. Drawbacks to the device include reduced excitation efficiency and higher-order mode excitation within the transmitter die. Most importantly, the source has demonstrated the unique ability to optoelectronically excite the TEM-mode of a 2D interconnect in a powerful manner with and without an applied bias. The PPT source was combined with a standard detector to demonstrate the direct excitation and detection of an air-filled parallel plate waveguide as a viable means of coupling an ultrafast THz pulse from point-to-point in a completely guided manner. With further experimental and theoretical consideration, the PPT transmitter, and its use within a larger 2D quasioptical structure, could find utility in THz research and commercial applications.

Chapter 5

Conclusions

This document has described several new contributions in guided wave THz research. A 2D quasioptical structure has been proposed and implemented. Within a sub-wavelength thickness, air-filled structure, 2D quasioptical elements have been shown to work as their 3D analogs in free space. These structures guide sub-ps pulses of THz radiation in both directions orthogonal to the direction of propagation while maintaining propagation in the low-loss and dispersion free TEM-mode. A new class of THz source has been developed to work directly with the new guiding structure to reduce or eliminate the need for quasioptically coupling these guiding structures to a larger external quasioptical circuit. The direct optoelectronic detection of the guided modes of the structure has also been demonstrated. Thus, a basic set of 2D components required to develop a planar analog of the THz systems used for the last two decades has been demonstrated. A fully integrated source, guiding structure, and detector have been demonstrated individually and together as viable candidates for the realization of ultra-high bandwidth circuitry.

In the first portion of this work, the theoretical basis of a 2D TEM-mode integrated optical structure was established. A basic premise was established on which the remaining experimental studies were founded. Some practical considerations regarding the fabrication of integrated quasioptical elements were also considered. The demonstration of the 2D guiding structure was carried out first using multiple reflections from incorporated flat mirrors to identify any deleterious effects of incorporating quasioptical elements within the guiding structure. Indeed, no such effects were observed. The demonstration proceeded to show the focusing action of a simple circular reflective element corresponded well with that expected from standard Fourier analysis. The transmissive and diffractive elements of a collaborating author were likewise shown to behave as expected by free space quasioptical theory. The demonstration of these individual elements has shown that a "2D optical table" may be fabricated to propagate sub-ps pulses of THz frequency radiation for arbitrarily long distances via complex pathways in the TEM-mode.

The second portion of this work described the development of a simple THz transmitter that not only directly couples to the 2D quasioptical structures described previously, but does so in a very powerful manner. As demonstrated in this work, the PPT transmitter generates a signal with amplitude comparable to the maximum signals recorded in our labs. The transmitter does so using non-ideal coupling optics and much more crude fabrication techniques than our current standard devices. The device is shown to be a powerful source of guided wave THz radiation in both biased and unbiased modes of operation, a feature that is unique and important among THz sources. The PPT transmitter has also demonstrated a wider FWHM bandwidth than standard devices (for a particular receiver geometry), with the gain in spectrum lying in the lower frequency range. The signal generated by the PPT transmitter was shown to directly couple to the TEM-mode of a parallel plate structure and to be optoelectronically detected by a modified standard receiver.

The 2D integrated quasioptical elements demonstrated in this work show great promise for directing sub-ps pulses through a complex circuit incorporating reflective, transmissive, and diffractive elements. Such a device may find use in very high-bandwidth, highly parallel board level circuits or as rugged waveguide based THz-TDS sensors. The PPT transmitter described in this work may also be used to directly excite these structures in a way that couples their further research to the anticipated behaviors of very fast chip level circuitry. Moreover, the PPT transmitter may find immediate application in free space or guided wave THz research situations where signal amplitude or fabrication complexity are the primary limiting factors on available transmitters. Lastly, the coupling of these two technologies into a completely integrated THz circuit could expand the advantages of THz time-domain techniques to a broader research community and perhaps commercial applications in a similar vein to integrated optical components at light frequencies.

References

1. W. Ryu, J. Lee, H. Kim, S. Ahn, N. Kim, B. Choi, D. Kam, and J. Kim, "RF interconnect for multi-Gbit/s board-level clock distribution," *IEEE Trans. Adv. Pack.* **23**, 398 (2000), *also see Ref.* [6].
2. Jianquan Zhang and D. Grischkowsky, "Waveguide THz time-domain spectroscopy,"*Opt. Lett.* to be published (2004).
3. M. Rochat, M. Beck, J. Faist, U. Oesterle, "Measurement of far-infrared waveguide loss using a multisection single-pass technique," *Appl. Phys. Lett.* **78**, 1967 (2001).
4. see for instance: M. B. Ketchen, D. Grischkowsky, T. C. Chen, C-C Chi, I. N. Duling, III, N. J. Halas, J-M. Halbout, J. A. Kash, G. P. Li, "Generation of sub-picosecond electrical pulses on coplanar transmission lines," *Appl. Phys. Lett.* **48**, 751 (1986).
5. K. J. Herrick, T. Schwarz, L. P. B. Katehi, "W-band micromachined finite ground coplanar (FGC) line circuit elements," *IEEE MTT-S Int. Microwave Symp. Dig.*, vol. 1, 269, Denver, CO, June 1997
6. for a comprehensive review of the search for an ultrawideband transmission channel preceding the demonstration of parallel plate structures, see: G. Gallot, S. P. Jamison, R. W. McGowan, and D. Grischkowsky, "Terahertz Waveguides," *J. Opt. Soc. Am. B*, **17** 851 (2000) and D. R. Grischkowsky, "Optoelectronic

characterization of transmission lines and waveguides by Terahertz time-domain spectroscopy," *IEEE Sel. Top. Quan. Elec.* **6**, 1122 (2000).

7. J. P. Becker, J. R. East, and L. P. B. Katehi, "Performance of silicon micromachined waveguide at W-band," *Elec. Lett.* **38**, 638 (2002).
8. J. Weinzierl, Ch. Fluhrer, H. Brand, "Dielectric waveguides at submillimeter wavelengths, *IEEE 6th Intl. Conf. THz Elec.*, 166, Leeds, UK, Sept. 1998.
9. S. Hirsch, Q. Chen, K. Duwe, R. Judaschke, "Design and Characterization of coplanar waveguides and filters on thin dielectric membranes at D-band frequencies," *IEEE 4th Intl. Kharkov Symp. Phys. Eng. mm sub-mm waves*, 678, Kharkov, Ukraine, June 2001.
10. R. Mendis and D. Grischkowsky, "Undistorted guided wave propagation of sub-picosecond THz pulses," *Opt. Lett.* **26**, 846 (2001).
11. R. Mendis and D. Grischkowsky, "THz interconnect with low loss and low group velocity dispersion," *IEEE Microw. Wirel. Comp. Lett.* **11**, 444 (2001).
12. E. Garmire, T. McMahon, and M. Bass, "Flexible infrared waveguides for high-power transmission," *IEEE J. Quant. Elec.* **QE-16**, 23 (1980).
13. J. W. Mink and F. K. Schwering, "A Hybrid dielectric slab-beam waveguide for the sub-millimeter wave region, *IEEE Trans. Microwave Theory Tech.* **41**, 1720 (1993).
14. S. Zeisberg, A. Schuenemann, G. P. Monahan, P. L. Heron, M. B. Steer, J. W. Mink, F. K. Schwering, "Experimental investigation of a quasi-optical slab resonator," *IEEE Microwave Guided Wave Lett.***3**, 253 (1993).

15. R. Kompfner, “Optics at Bell Laboratories-Optical Communications,” *Appl. Opt.* **11**, 2412 (1972).
16. S. E. Miller, “A survey of integrated optics,” *IEEE J. Quant. Elec.* **QE-8**, 199 (1972)
17. R. Shubert and J. H. Harris, “Optical guided-wave focusing and diffraction,” *J. Opt. Soc. Am.* **61**, 154 (1971), and references therein.
18. R. Ulrich and R. J. Martin, “Geometrical optics in thin film light guide,” *Appl. Opt.* **10**, 2077 (1971).
19. D. B. Anderson, R. L. Davis, J. T. Boyd, and R. R. August, “Comparison of optical-waveguide lens technologies,” *IEEE J. Quant. Elec.* **QE-13**, 275 (1977).
20. T. Suhara, K. Kobayashi, H. Nishihara, and J. Koyama, “Graded-index Fresnel lenses for integrated optics,” *Appl. Opt.* **21**, 1966 (1982).
21. V. A. Bhagavatula, R. O. Maschmeyer, R. J. Haggerty, P. A. Sachenik, and G. T. Holmes, “Planar lens devices by CVD process,” *Electronic Components and Technology Conf. Proc.* **43** 1-4 June 1993.
22. H. P. Zappe, *Introduction to Semiconductor Integrated Optics* (Artech House, Boston, USA 1995).
23. N. S. Stoyanov, D. W. Ward, T. Feurer, and K. A. Nelson, “Terahertz polariton propagation in patterned materials,” *Nat. Mat.* **1**, 95 (2002).
24. N.S. Stoyanov, T. Feurer, D. W. Ward, and K. A. Nelson, “Integrated diffractive THz elements,” *Appl. Phys. Lett.* **82**, 674 (2003).
25. D. W. Ward, E. Statz, J. D. Beers, N. Stoyanov, T. Feurer, R. M. Roth, R. M. Osgood, and K. A. Nelson, “Phonon-polariton propagation, guidance, and control

in bulk and patterned thin film ferroelectric crystals," *Mat. Res. Soc. Symp. Proc.* **797**, W5.9.1 (2004).

26. R. Mendis and D. Grischkowsky, "Plastic ribbon THz waveguides," *J. Appl. Phys.* **88**, 4449 (2000).
27. M. Lax, W. H. Louisell, and W. B. McKnight, "From Maxwell to paraxial wave optics," *Phys. Rev. A* **11**, 1365 (1975).
28. D. M. Pozar *Microwave Engineering 2nd Ed.* (New York, John Wiley and Sons, 1998).
29. G. P . Agrawal *Fiber-Optic Communication Systems 2nd Ed.* (New York, John Wiley and Sons, 1997).
30. B. E. A. Saleh and M. C. Teich *Fundamentals of Photonics* (John Wiley and Sons, USA 1991).
31. A. E. Siegman *Lasers* (University Science Sausalito, USA 1986).
32. D. H. Martin and J. W. Bowen, "Long-wave optics," *IEEE Trans. Microwave Theory Tech.***41**, 1676 (1993).
33. P. F. Goldsmith *Quasioptical Systems* (IEEE Press/Chapman and Hall New York, USA 1998).
34. J. LeSurf *Millimetre-Wave Optics, Devices, and Systems* (IOP Publishing New York 1990).
35. J. W. Goodman *Introduction to Fourier Optics* (McGraw-Hill Intl. Singapore 1968).

36. M. O'Donnel, E. T. Jaynes, and J. G. Miller, "Kramers-Kronig relationship between ultrasonic attenuation and phase velocity," *J. Acoust. Soc. Am.* **69**. 696 (1981).
37. R. A. Abram and G. J Rees, "Mode conversion in an imperfect waveguide," J. Phys. A: Math., Nucl. Gen. **6**, 1693 (1973).
38. A. Wexler, "Solution of waveguide discontinuities by modal analysis," *IEEE Trans. Microwave Theory Tech.* **15**, 508 (1967).
39. A. Taflove and S. C. Hagness *Computational Electrodynamics* (Boston, Artech House, 2000).
40. M. N. O. Sadiku, *Numerical Techniques in Electromagnetics, 2nd Ed.* (New York, CRC Press, 2000).
41. K. S. Yee, "Numerical solution to initial boundary-value problems involving Maxwell's equations in isotropic media," *IEEE Trans. Ant. Prop.* **AP-14**, 302 (1966).
42. C. A. Balanis *Antenna Theory Analysis and Design* (John Wiley New York, USA 1997).
43. W. V. Andrew, "tehorn.m", MATLAB M-file included with [42] above (1995).
44. J. Schwinger and D. S. Saxon, *Discontinuities in Waveguides* (New York, Gordon and Breach, 1968).
45. N. Marcuvitz *Waveguide Handbook* (London, U. K.: Peter Peregrinus, 1993).
46. R. E. Collin *Field Theory of Guided Waves, 2nd Ed.* (New York, USA, IEEE Press/John Wiley and Sons, 1991).

47. F. Alessandri, G. Bartolucci, and R. Sorrentino, “Admittance matrix formulation of waveguide discontinuity problems, computer-aided design of branch guide directional couplers,” *IEEE Trans. Microwave Theory Tech.* **36**, 394 (1988).
48. S. Coleman and D. Grischkowsky, “A THz transverse electromagnetic mode two-dimensional interconnect layer incorporating quasioptics,” *Appl. Phys. Lett.* **83**, 3656 (2003).
49. J. Dai, S. Coleman, and D. Grischkowsky, “Planar THz quasioptics,” *Appl. Phys. Lett* **85,** 884 (2004).
50. M. T. Reiten, S. A. Harmon, and R. A. Cheville, “Terahertz beam propagation measured through three-dimensional amplitude profile determination,” *J. Opt. Soc. Am. B* **20**, 2215 (2003).
51. H. Urey, “Spot size, depth-of-focus, and diffraction ring intensity formulas for truncated Gaussian beams,” *Appl. Opt.* **43**, 620 (2004).
52. J. Birch, “The far infrared optical constants of polyethylene,” *Infrared Phys.* **30**, 195 (1990)
53. H. Cao, R. A. Linke, and A. Nahata, “Phase-matched generation of broadband terahertz radiation in a waveguide,” *Conference on Lasers and Electro-Optics Conference Proceedings*, CMB1, June 1-6 (2003).
54. H. Cao, R. A. Linke, and A. Nahata, “Broadband generation of terahertz radiation in a waveguide,” *Opt. Lett.* **29**, 1751 (2004).
55. S. Coleman and D. Grischkowsky, “Parallel Plate THz Transmitter,” *Appl. Phys. Lett,* **84**, 654 (2004).

56. R. A. Cheville performed the metallization and dicing experiment for the E-beam evaporated PPT devices.
57. R. F. Harrington, *Time-Harmonic Electromagnetic Fields* (IEEE Press/John Wiley, New York, USA 2001).
58. J. R. Tessman and J. T. Finnel Jr., "Electric field of an accelerating charge," *Am. J. Phys.* **35**, 523 (1967).
59. S. E. Ralph and D. Grischkowsky, "Trap-enhanced electric fields in semi-insulators: The role of electrical and optical carrier injection," *Appl. Phys. Lett.* **59**, 1972 (1991).
60. O. Svelto *Principles of Lasers* (Plenum New York, USA 1998).
61. M. Haiml, U. Siegner, F. Morier-Genoud, U. Keller, M. Luysberg, R. C. Lutz, P. Specht, E. R. Weber, "Optical nonlinearity in low-temperature-grown GaAs: Microscopic limitations and optimization strategies," *App. Phys. Lett.* **74**, 3134 (1999).
62. while none of the literature I have found examines field screening as a function of pulse fluence, the concepts of field screening may be examined in: U. D. Keil, D. R. Dykaar, R. F. Kopf, and S. B. Darack, "Reflectivity measurements of femtosecond carrier and field dynamics in semiconductors," *Appl. Phys. Lett.* **64**, 3267 (1994) or M. D. Cummings, J. F. Holzman, A. Y. Elezzabi, "Femtosecond carrier dynamics in an asymmetrically excited GaAs photoconductive switch," *Appl. Phys. Lett.* **78**, 3535 (2001).
63. S. M. Sze *Physics of Semiconductor Devices 2nd Ed.* (John Wiley & Sons New York, USA 1981).

64. H. Cao, T. F. Heinz, A. Nahata, “Electro-optic detection of femtosecond electromagnetic pulses by use of poled polymers,” Opt. Lett. **27**, 775-777 (2002).
65. E. H. Rhoderick and R. H. Williams *Metal-Semiconductor Contacts* p.9 (Oxford Press, New York, USA 1988).

VITA

Steven Michael Coleman

Candidate for the Degree of

Doctor of Philosophy

Thesis: 2D TEM-MODE THz QUASIOPTICS

Major Field: Photonics

Biographical:

Education: Graduated as valedictorian from Carl Albert High School, Midwest City, Oklahoma in May 1995; received Bachelor of Science Degree w/ Honors in Electrical Engineering from Oklahoma State University, Stillwater, Oklahoma in May 2000. Completed the requirements for the Doctor of Philosophy degree with a major in Photonics in May 2005.

Experience: Employed by Nomadics, Inc., Stillwater, Oklahoma as an engineering assistant from 1997 to 1999; Sciperio, Inc., Stillwater, Oklahoma as (Electrical) Engineer II from 1999 to 2002; Doctoral fellow at the Ultrafast Terahertz Optoelectronic Laboratory, Oklahoma State University from 2002 to 2004. Northrop Grumman Space Technology, St. Charles, Missouri as Laser Engineer from 2004 to present.

Awards: National Science Foundation IGERT Fellowship from 2000 to 2004; US Patent Number 6,663,793: “Sol-Gel-Based Materials for Direct-Write Electronics Applications”

Name: Steven Michael Coleman Date of Degree: May, 2005

Institution: Oklahoma State University Location: Stillwater, Oklahoma

Title of Study: 2D TEM-MODE THZ QUASIOPTICS

Pages in Study: 109 Candidate for the Degree of Doctor of Philosophy

Major Field: Photonics

Scope of Study: The purpose of this study was to develop a two-dimensional wave guiding structure incorporating quasioptical mirrors, lenses, diffractive elements, sources and detectors for ultrafast pulses of THz radiation. Design curves allow rapid system development under various constraints. The theory governing the behavior of quasioptical components in the overall guiding structure is developed and first-order approximations are made for the effects of certain non-idealities expected in fabrication. Reflective, transmissive, and diffractive elements are demonstrated and analyzed. A new type of ultrafast source, adapted to the guiding structure has also been developed. A preliminary demonstration of guided-wave TEM-mode point-to-point communication using the new source is made.

Findings and Conclusions: Standard quasioptical techniques are found to be valid approximations for TEM-mode guided radiation for distances to several meters. The most significant issue in fabrication of integrated TEM-mode optics is found to be gaps between the elements and guide plates. Tilted mirrors may be used as mode converters within the waveguide. 2D integrated quasioptical mirrors, lenses, and slits were found to perform as expected for the analogous 3D device in unbounded space, as predicted. The new source was found to be a simple, powerful source in both free space and within the new guiding structure. The source was demonstrated to work as a useful THz source via photoconductive switching and optical rectification. Standard receivers were shown to work as detectors for the guided TEM-mode. In this work, the individual components of a point-to-point TEM-mode communication system for ultrafast pulses of THz radiation are demonstrated.

ADVISER'S APPROVAL: Daniel R. Grischkowsky